

# Synthesis and resistive switching properties of nickel oxide nanostructures made via a phase separation approach

**Author:**

Sullaphen, Jivika

**Publication Date:**

2012

**DOI:**

<https://doi.org/10.26190/unsworks/15561>

**License:**

<https://creativecommons.org/licenses/by-nc-nd/3.0/au/>

Link to license to see what you are allowed to do with this resource.

Downloaded from <http://hdl.handle.net/1959.4/52005> in <https://unsworks.unsw.edu.au> on 2024-05-05

**Synthesis and resistive switching properties of  
nickel oxide nanostructures  
made via a  
phase separation approach**

A Thesis

By

**Jivika Sullaphen**

Supervisor: Associate Professor Nagarajan Valanoor

Submitted in Partial Fulfilment of the  
Requirement for the Degree of  
Masters of Philosophy  
in  
Materials Science

School of Materials Science and Engineering  
University of New South Wales

March 2012

## **CERTIFICATE OF ORIGINALITY**

I hereby declare that this submission is my own work and to the best of my knowledge it contains no materials previously published or written by another person, nor materials which to a substantial extent has been accepted for the award of any other degree or diploma and UNSW or any other educational institution, except where due acknowledgment is made in the thesis. Any contribution made to the research by others, with whom I have worked at UNSW or elsewhere, is explicitly acknowledged in the thesis.

I also declare that the intellectual content of the thesis is the product of my own work, except to the extent that the assistance from others in the project's design and conception or in style, presentation and linguistic expression is acknowledged.

(Signed) .....

(Date) .....

## **ACKNOWLEDGEMENTS**

I would like to convey my appreciation to everyone who influenced and encouraged me in some way throughout the duration of my masters course. It is a pleasure to thank you for your time, assistance and contributions towards making this thesis possible.

First and foremost I would like to thank my supervisor, Associate Professor Nagarajan Valanoor for giving me the opportunity to take on this project and assisting with TEM images, etc.. His time and effort to explain concepts clearly has made this an invaluable experience.

I owe my deepest gratitude to Dr. Kashinath Bogle who assisted me throughout each stage of this project. His training, helpful advice and guidance have been of great assistance. I would also like to thank all members of our research group, especially Heidi for her TEM work and great advice; Jeff for his help on countless occasions and interesting discussions; and Jason for his helpful advice and entertaining comments. Thank you for providing a fun and helpful environment.

I am grateful to the electron microscope unit and solid state elemental analysis unit for providing the necessary resources. Thank you Eugene White, Deming Zhu, Katie Levick, Sean Lim and Dr. Yu Wang for the training and help on the equipment.

I would also like to extend a great thanks to my friends and family for their support, care, motivation and amusing conversations. A special thanks goes to my parents for caring, supporting, encouraging and putting up with me throughout the years.

## ABSTRACT

This thesis investigates the synthesis and resistive switching properties of nickel oxide (NiO) nanostructures grown on strontium titanate, SrTiO<sub>3</sub> and niobium doped SrTiO<sub>3</sub> substrates of (001) orientation a phase separation approach. Pulsed laser deposition of a bismuth nickel oxide (BiNiO<sub>3</sub>) perovskite precursor is carried out under conditions which induce perovskite decomposition into bismuth oxide and NiO. Post-deposition process conditions are then finetuned to exploit the volatile nature of bismuth oxide which then leaves behind an array of self-assembled NiO nanostructures.

Varying synthesis parameters allows us to find the optimum conditions for controlling the morphology and chemical properties. Firstly deposition partial O<sub>2</sub> pressures were examined to show the influence on the morphology and phase of the samples. Results show the optimum pressure to be 50 mTorr. Next the temperature was modified. A substantial effect was observed with both crystal shape and inter-particle distance. The 900 °C sample was shown to be the optimum temperature. The influence of laser pulses on volume and nanocrystal shape was then investigated. 5 000 pulses showed the formation of square pyramidal hut shaped structures, 10 000 showed some hut shapes as well as truncated pyramids and 20 000 showed a film-like growth indicating a metastable state of joined hexagonal structures. Finally the effects of annealing conditions were considered. Samples annealed in a vacuum showed round structures composed of Ni<sub>2</sub>O<sub>3</sub>. 100 mTorr O<sub>2</sub> partial pressure showed NiO phases however the structures were undefined and 1 Torr was found to promote formation of defined nanostructures and NiO(200) phase constituents.

In understanding the resistive switching properties of these individual nanostructures conductive– atomic force microscopy was used. The role of the interface as well as the

interplay between the nanostructure morphology and resistive switching properties and the governing mechanisms are required in order to create efficient switching devices based on nickel oxide. We find that the nanostructures display prominent extrinsic bipolar switching characteristics in a specific height range ( $\sim 20$ - $15$  nm). Heights lower than this show conductive behaviour and taller heights display a strong rectifying behaviour. The maximum ON/OFF ratio is at  $\sim 10^3$  at a read voltage of  $\sim +0.4$  V. This ratio is found to decrease with increasing height of the nanostructure. Linear fittings of I-V loops reveal that low and high resistance states follow Ohmic-conduction and Schottky-emission mechanism, respectively. This switching behaviour (dependence on height) is attributed to the modulation of the carrier density at the nanostructure-substrate interface due to the applied electric field.

## TABLE OF CONTENTS

CERTIFICATE OF ORIGINALITY .....	II
ACKNOWLEDGEMENTS .....	III
ABSTRACT .....	IV
LIST OF FIGURES .....	IX
LIST OF TABLES .....	XII
LIST OF EQUATIONS .....	XIII
LIST OF APPENDICES .....	XIV
CHAPTER 1. INTRODUCTION .....	1
CHAPTER 2. LITERATURE SERVEY .....	3
2.1. Properties of Nickel Oxide .....	3
2.2. Applications of Nickel Oxide .....	4
2.3. Resistive Switching .....	6
2.4. Growth (Deposition) Techniques .....	8
2.4.1. Pulsed laser Deposition (PLD) .....	12
2.5. Characterisation Techniques .....	15
2.5.1. Atomic Force Microscopy (AFM) .....	16
2.5.2. X-Ray Diffraction (XRD) .....	17
2.5.3. Scanning Electron Microscopy (SEM) .....	19
I. Energy Dispersive Spectroscopy (EDS) .....	20
2.5.4. Transmission Electron Microscopy (TEM) .....	20

CHAPTER 3. EXPERIMENTAL PROCEDURE.....	22
3.1. Phase Separation Approach.....	22
3.2. Reflection High Energy Electron Diffraction (RHEED) analysis.....	23
3.3. Sample Preparation.....	25
3.3.1. Synthesis Method .....	25
I. Pulsed Laser Deposition (PLD).....	25
A. Deposition .....	25
B. Post Deposition Annealing.....	27
3.3.2. Characterisation Preparation .....	27
I. AFM .....	27
II. XRD.....	28
III. SEM.....	29
A. EDS .....	29
IV. TEM.....	29
CHAPTER 4. RESULTS AND DISCUSSION.....	30
(SYNTHESIS OF NICKEL OXIDE NANOSTRUCTURES) .....	30
4.1. Understanding the role of synthesis parameters.....	30
4.1.1. Varying the Deposition Pressure .....	32
4.1.2. Varying the Deposition Temperature .....	42
4.1.3. Varying the Number of Laser Pulses .....	49
4.1.4. Varying the chamber pressure during Annealing.....	53

CHAPTER 5. RESULTS AND DISCUSSION.....	57
(RESISTIVE SWITCHING EFFECT) .....	57
5.1. I-V measurements.....	57
5.2. Resistive Switching Mechanism .....	61
5.3. A detailed analysis of the conduction mechanism in NiO/Nb:STO.....	63
CHAPTER 6. CONCLUSIONS .....	68
CHAPTER 7. PROSPECTS FOR FUTURE WORK.....	70
7.1. Varying the Substrate orientation.....	70
7.1.1. STO (111).....	70
7.1.2. STO (110).....	72
7.2. Incoherent interface on resistive switching effect.....	74
CHAPTER 8. REFERENCES .....	75
APPENDICES .....	i

## LIST OF FIGURES

<b>Figure 2.1-1.</b> NiO cubic rock salt structure[16].	3
<b>Figure 2.3-1.</b> I-V loops for the (a) unipolar mechanism (b) for a bipolar mechanism [36].	7
<b>Figure 2.4-1.</b> Flowchart showing the classes of deposition techniques	11
<b>Figure 2.4.1-1.</b> (a) Neocera Cluster II PLD system (b) a diagrammatic representation of a PLD system [63].	13
<b>Figure 3.1-1.</b> Schematic representation of the phase separation approach [82]. (a) Step 1: Synthesis approach (b) Step 2: Bismuth oxide removal.	23
<b>Figure 3.2-1.</b> RHEED pattern for (a) blank STO – before deposition (b) NiO after deposition (c) NiO after cooling down (d) corresponding diffraction pattern taken from Webemaps.	24
<b>Figure 4.1.1-1.</b> Sample images for depositing in 10 mTorr O <sub>2</sub> , 5 000 pulses, 860 °C and annealing in 1 Torr O <sub>2</sub> on STO (001) (a) SEM (b) XRD pattern (c) AFM (d) EDS using SEM	33
<b>Figure 4.1.1-2.</b> Sample images for depositing in 35 mTorr O <sub>2</sub> , 5 000 pulses, 860 °C and annealing in 1 Torr O <sub>2</sub> on STO (001) (a) SEM (b) XRD pattern (c) AFM (d) EDS using SEM (e) size analysis.	34
<b>Figure 4.1.1-3.</b> Sample images for depositing in 50 mTorr O <sub>2</sub> , 5 000 pulses, 860 °C and annealing in 1 Torr O <sub>2</sub> on STO (001) (a) SEM (b) AFM (c) size analysis (d) TEM (e) TEM diffraction pattern (f) XRD pattern (g) EDS using SEM.	37
<b>Figure 4.1.1-4.</b> Sample images for depositing in 100 mTorr O <sub>2</sub> , 5 000 pulses, 860 °C and annealing in 1 Torr O <sub>2</sub> on STO (001) (a) SEM (b) AFM (c) Size analysis (d) XRD pattern.	39

<b>Figure 4.1.1-5.</b> Comparing the pressure variations (a) Height frequency distribution: (b) L/W as a function of volume .....	40
<b>Figure 4.1.2-1</b> Sample images for depositing in 50 mTorr O <sub>2</sub> , 5 000 pulses, 900 °C and annealing in 1 Torr O <sub>2</sub> on STO (001) (a) SEM (b)AFM (c) Size analysis plot (d) TEM diffraction pattern (e) HR-TEM (f) XRD pattern. ....	42
<b>Figure 4.1.2-2.</b> Sample images for depositing in 50 mTorr O <sub>2</sub> , 5 000 pulses, 900 °C and annealing in 1 Torr O <sub>2</sub> on STO (001) (a) EDS using SEM (b) EDS line scans using TEM (c) XRD pattern.....	45
<b>Figure 4.1.2-3.</b> Comparing the temperature variations: height frequency distribution..	48
<b>Figure 4.1.2-4.</b> Comparing the temperature variations as a function of volume (a) L/W (b) L/H.....	48
<b>Figure 4.1.3-1.</b> Sample images for depositing in 50 mTorr O <sub>2</sub> , 10 000 pulses, 900 °C and annealing in 1 Torr O <sub>2</sub> on STO(001) (a) SEM (b) AFM (c) XRD. ....	51
<b>Figure 4.1.3-2.</b> Sample images for depositing in 50 mTorr O <sub>2</sub> , 20 000 pulses, 900 °C and annealing in 1 Torr O <sub>2</sub> on STO(001) (a) SEM (b) AFM (c) XRD. ....	52
<b>Figure 4.1.4-1.</b> Sample images for depositing in 35 mTorr O <sub>2</sub> , 10 000 pulses, 860 °C and annealing in a vacuum on STO (001) (a) SEM before annealing (b) XRD pattern before annealing (c) SEM after annealing (d) XRD pattern after annealing. ....	54
<b>Figure 4.1.4-2.</b> Sample images for depositing in 50 mTorr O <sub>2</sub> , 5 000 pulses, 860 °C and annealing in 100 mTorr O <sub>2</sub> and 1 Torr O <sub>2</sub> on STO (001) (a) SEM before annealing (b) XRD before annealing (c) SEM after annealing in 100 mTorr O <sub>2</sub> (d) XRD after annealing in 100 mTorr O <sub>2</sub> (e) SEM after annealing in 1 Torr O <sub>2</sub> (f) XRD after annealing in 1 Torr O <sub>2</sub> . ....	55
<b>Figure 5.1-1.</b> Resistive switching characteristics of the NiO nanostructures. (a) I-V measurements (b) ON/OFF ratio versus height. ....	58

<b>Figure 5.1-2.</b> Resistive switching characteristics of an individual NiO nanostructure. (a) Points 1 – 4 are various heights along an individual nanostructure. (b) I-V measurements taken at points 1-4 from..	60
<b>Figure 5.1-3.</b> ON/OFF ratio vs. Lateral area plot.	61
<b>Figure 5.2-1.</b> Linear fitting results of (a) LRS in bipolar switching with Ohmic conduction and (b) for HRS which show Schottky emission conduction behavior in a 15 nm high nanostructure.	63
<b>Figure 5.3-1.</b> Schematic of conduction mechanism in NiO/Nb:STO p-n junction and its respective band diagram at zero bias (a) and (b), forward bias (c) and (d), and reverse bias (e) and (f). Width of depletion region has been calculated for 1 V applied in forward and reverse bias.	65
<b>Figure 7.1.1-1.</b> Sample images for depositing in 50 mTorr O <sub>2</sub> , 5 000 pulses, 900 °C and annealing in 1Torr O <sub>2</sub> STO (111) (a) SEM (b) XRD pattern (c) AFM (d) EDS using SEM.	71
<b>Figure 7.1.2-1.</b> Sample images for depositing in 50 mTorr O <sub>2</sub> , 5 000 pulses, 900 °C and annealing in 1Torr O <sub>2</sub> STO (110) (a) SEM (b) XRD pattern (c) AFM.(d) EDS using TEM (e) TEM image of NiO nanostructure (f) electron diffraction pattern.	73
<b>Figure 7.1.2-2.</b> EDS mapping data for (a) Nickel (b) TEM image of NiO nanostructure (c) Strontium (d) Titanate (e) Oxygen.	74

## LIST OF TABLES

<b>Table 4.1-1.</b> Deposition and Annealing Conditions .....	31
<b>Table 4.1.2-1.</b> Parameters calculated for misfit strain and lattice parameters.....	47

## LIST OF EQUATIONS

<b>Equation 2.5.1-1.</b> Bragg's condition [75].	18
<b>Equation 4.1.2-1.</b> In plane lattice strain for the NiO - STO lattice.	46
<b>Equation 4.1.2-2.</b> Lattice strain using the Poisson ratio..	46
<b>Equation 4.1.2-3.</b> Out of plane lattice strain for the out of plane NiO lattice parameter.	47
<b>Equation 5.2-1.</b> Space charge limited (SCL) conduction.	61
<b>Equation 5.2-2.</b> Schottky emission (SE).	62
<b>Equation 5.2-3.</b> Poole-Frenkel (PF) emission.	62
<b>Equation 5.3-1, 5.3-2.</b> Depletion width..	64

## **LIST OF APPENDICES**

<b>APPENDIX A</b> – Blank STO (substrate) XRD peaks .....	i
<b>APPENDIX B</b> – Substrate holder XRD peaks .....	ii

## CHAPTER 1. INTRODUCTION

Nanostructured metal oxides have the ability to crystallize into a variety of structures containing a high density surface area to volume ratio and therefore possess a range of unique chemical, mechanical and physical properties ranging from electric/dielectric, optical and magnetic to a reversible oxidation - reduction processes occurring from the absorption of specific gasses [2; 25; 71]. Such properties are fine-tuned by varying the shape and size of the nanostructure. These nanostructures include nanoparticles, nanotubes, nanowires, nanobelts nanorods, nanocubes and nanotubes [53; 71]. Metal oxides are also found to have extraordinary metal-insulator transitions relying on the temperature, magnetic field or pressure [63] thus making them appealing towards a variety of applications. Some of the metal oxides that are used in applications such as solar cells, electronics, semiconductors, gas and chemical sensors, optical sensors, batteries, varistors, catalysis, and non-volatile storage media include iron, copper, nickel, manganese, cobalt, titanium, bismuth, magnesium and zinc oxide [46].

In conjunction, transition metal oxides have gained interest due to its defect induced self doping capabilities and a partially filled d-orbital [71]. The nature of cation-oxygen bonding in transitional metal oxides reveal a wider range of electronic properties (showing either metallic, semiconductor or insulator characteristics) [25; 63].

Nickel oxide (NiO) is one such binary transition metal oxides of interest at present. NiO has attracted attention specifically due to its catalytic, electronic, optical and magnetic properties [59; 84]. The simple cubic rock-salt structure and wide intrinsic energy gap of  $\sim 4$  eV [24] makes NiO appealing towards range of applications such as electrochemical capacitor material [91], sensing materials in gas and humidity detection

devices [20; 23], optical fibres [70], and particularly resistive switching applications (non-volatile storage media) [50].

The focus of this thesis is on the synthesis and functional characterisation of NiO nanostructures fabricated from a bismuth nickel oxide precursor using pulsed laser deposition. Strontium titanate (STO) of (001) orientation was used as the substrate. The role of process parameters including deposition O<sub>2</sub> partial pressure, temperature, laser pulses or annealing chamber O<sub>2</sub> partial pressure were studied in order to obtain optimised nanostructures. The correlation between these conditions, the sample chemistry and morphology was then analysed using specific characterisation tools such as the scanning electron microscope (SEM), atomic force microscope (AFM), transmission electron microscope (TEM), electron dispersive spectroscopy (EDS) and x-ray diffraction (XRD). Each of these techniques is elaborated on in further sections.

The size-dependent (in particular island height dependence) resistive switching is then examined in the optimised sample, which is comprised of epitaxial NiO islands on niobium doped STO (Nb: STO). Non-volatile resistance switching characteristics of the NiO nanostructures were studied using conductive-AFM. A distinct extrinsic bipolar switching nature is observed for islands of a particular height range (~ 10-23 nm). No switching is observed for islands below or above this height range, the respective behaviour being conductive and resistive. Numerical fitting and analysis of the I-V response strongly suggests that the resistive switching is due to the modulation of the bottom interface, where the applied electric field controls the minority carrier distribution and hence alters conductivity.

## CHAPTER 2. LITERATURE SERVEY

### 2.1. Properties of Nickel Oxide

Nickel oxide, NiO, also known as bunsenite in its pure form is a p-type semiconductor with a molecular weight of 74.71g/mol, and a melting point of 1990 °C [58]. This wide band gap, binary metal oxide, has a reported bandgap of ~4.0 eV [24] and a 6 coordinate (octahedral) geometry [89] as shown below in figure 2.1-1.

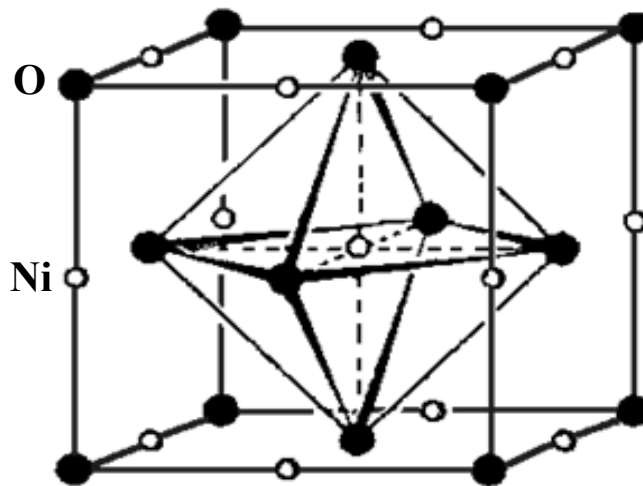


*Figure 2.1-1. Diagrammatic representation of the NiO cubic rock salt structure [89].*

It has been proposed that the enhanced p-type conductivity in NiO is a result of nickel vacancies and excess oxygen in interstitial sites resulting in its excellent electrochemical stability [4]. NiO retains properties such as good crystallinity and controllable transmittance for incident visible light [52]. When combined with alloys the resultant properties include a high fusion temperature and good oxidation and corrosion resistance. It has also been known to enhance the magnetic and electrical properties of

ferrite compositions [33]. NiO is an antiferromagnetic material retaining a Néel temperature of 523 K [23; 84; 94], indicating that there is no gross external magnetism. The ions spontaneously align into anti-parallel assembly (neighbouring spins positioned in opposite directions) so that the ions in one direction will cancel out the opposing ions [13]. Above the Néel temperature the material will become paramagnetic. More recently NiO was found to have extraordinary resistive switching behaviours [51].

## **2.2. Applications of Nickel Oxide**

Due to its vast array of properties (mentioned above), NiO has been greatly exploited by numerous industries ranging from ceramics and materials engineering to electronic and chemical industries. NiO is used extensively in electrochromics and batteries [3; 12]. The experiments carried out by Azens show the effects of heating on the NiO film electrochromic activity for use as an electrode. Chen *et al.* demonstrate that the structural features of the RF sputtered NiO films influence the electrochromic properties. Another of the applications of nickel oxide, as demonstrated by Wu *et al.* [91], is that when nanoporous NiO film is electrochemically deposited onto a stainless steel substrate, a high charge/discharge capability is displayed as well as a stable capacitance during the cycles. They demonstrate that NiO films can enhance the electrochemical capacitance behaviour and therefore be used in electrochemical capacitor material, thermistors and varistors.

In the optimum conditions the synthesized NiO thin films exhibit high optical chattels. Many experiments have been carried out [77] to show the thermal stability up to 250°C on NiO films for an exchanged biased layer. NiO nanosized particles have also been

widely used in the consumer industry in magnets, batteries, stainless steel, alloys and plating [78].

Mattei *et al.* [56] synthesise nanoparticles containing a metal oxide and noble metal interface (NiO/Au) accessible to a certain gas in order to enhance the optical sensitivity (absorption of a gas). NiO can also be used along with acids to form salts and be doped with gold for electrodes in optoelectronic devices as well as in sensing materials found in chemoresistive or optical gas and humidity detection devices [23; 56]. Newman and Chrenko [62] have investigated the optical properties of NiO and its relevance in semiconductors and ferromagnets. The ability to selectively absorb light has been utilised as a colour pigment in glass [52]. Since NiO is relatively insoluble in glass, when combined with other elements can result in different colours. Colours used in art such as violet, blue, green, yellow, red, brown and grey have been reported in literature citations [33].

Dye sensitized solar cell have also been developed with mesoporous NiO thin films [42]. NiO based solar cells are shown to utilise an inverse working principle to the conventional n-type dye sensitized solar cells (DSSCs) [65; 68]. Other applications which utilise NiO include electro-chromic display devices, optical fibres, catalysts for CO oxidation, photo electrolysis, fuel cell electrodes and thermal solar cells [70].

A recent finding is that NiO plays a critical role in the resistive switching properties of high speed, high density non-volatile memory [1; 69]. Lee *et al.* [50] use the two oxide resistors: NiO and VO<sub>2</sub> in non-volatile memory. Here the NiO acts as a memory element to store data with a bi-stable resistance switching state and the VO<sub>2</sub> acts as a switch element to control access to a certain parts of the memory. NiO resistors are used because of its reversible and non-volatile switching behaviors between high resistance

states (HRS) and low resistance states (LRS). The robust processability of NiO as shown by Ahn *et al.* [1] is utilized in Resistance RAM (RRAM). NiO doped with titanium shows fast programming speeds and low writing currents.

In this thesis the resistance switching effect of the fabricated NiO nanostructures will be examined for potential use in non-volatile memory and RRAM applications. This effect is detailed in the next section.

### **2.3. Resistive Switching**

The resistance switching phenomenon occurs due to the effect of an applied electric field to show hysteric current-voltage (I-V) loops which consists of a sudden change in resistance. Resistance switching is most commonly found in metal-insulator-metal structures or metal-semiconductor-metal structures. The change resistive switching mechanism is denoted by two states; one being the high resistance state (HRS) and the other the low resistance state (LRS). The term ‘set switching’ is give to the movement from the HRS to the LRS, thereafter the term ‘reset switching’ is given to that from the LRS to HRS[41]. Reports on the resistive switching show two classifications of the switching mechanism, distinguished according to the way the bias is apply to change the resistance state. One is unipolar switching in which two stable resistance states can be achieved by switching voltage with the same polarity. Found mainly in highly insulating oxides, it occurs when the amplitude of the applied voltage influences the switching direction. The other is bipolar switching which requires switching the voltage with opposite polarities to induce bistable resistance states. Therefore this mechanism relies on the polarity of the applied voltage to manipulate the directional resistive switching and is generally found in semiconducting oxides [72]. Hence oxide materials

have been used extensively for this purpose. An example of the difference in switching is highlighted in the images shown in figure 2.3-1.

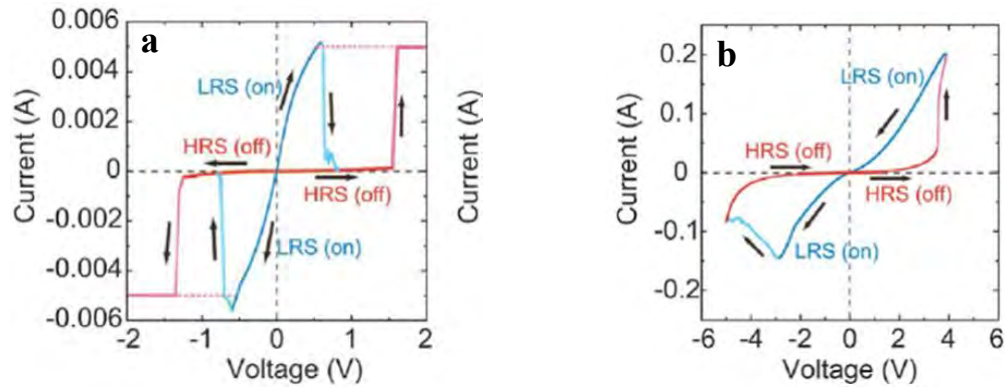


**Figure 2.3-1** *I-V loops for the (a) unipolar mechanism and (b) for a bipolar mechanism [72].*

The resistive switching effect, used as a basis for RRAM [47; 85] has been found in many transition metal oxides thin films such as  $\text{TiO}_2$  [8; 14],  $\text{CoO}$  [75],  $\text{ZrO}_2$  [92],  $\text{SrTiO}_3$  [80], and  $\text{NiO}$  [27; 51]. Given the demand for high-density memory, the focus has now shifted to nanoscale materials such as nanowires [64], nanocrystals [61] and ultra-thin films [73]. In particular,  $\text{NiO}$  shows the occurrence of this switching phenomenon in both its single and poly-crystalline nanoscale forms [73].

Reports on the resistive switching in epitaxially grown metal oxide thin films [36; 48; 51] explain the effect of synthesis conditions and type of electrodes on the resistive switching. Recent resistive switching studies on epitaxial  $\text{NiO}$  nanowire arrays [64; 87] using conductive atomic force microscopy (C-AFM) and a probe station equipped with a semiconductor parameter analyser respectively shows that the governing resistive

switching nature is bipolar. Studies on the electroforming behaviours of conducting nanofilaments in single crystalline NiO core/shell nanodisk arrays [39] using conducting AFM has reported influence of the contact time and area between the sample surface and the tip. In this thesis we show that the resistive I-V switching in epitaxial NiO nanostructures is influenced by the nanostructure morphology (in particular height) and that the interface between the substrate and the nanostructure plays a critical role in determining the magnitude of switching. This would therefore be ideal for non-volatile memory (such as flash memory, computer storage devices and ReRAM).

## **2.4. Growth (Deposition) Techniques**

As nanostructure synthesis is a significant component of this thesis, it is worth while reviewing material growth techniques. Thin film nanostructure deposition in general, refers to the addition of a material onto a surface or substrate resulting in the formation of nanostructures or a thin layer usually nanometers thick. Deposition techniques have also proved useful in the growth of nanostructures such as nanowires and carbon nanotubes, which form the basis of nanoelectronics, photonics, and bioengineering [95]. The different techniques used to fabricate nanostructures and thin films are explored here.

Thin films and nanostructures have many purposes in today's society expanding from household applications such as the mirror to drug delivery [30] in pharmaceuticals to optical and electronic devices [62]. Optics use thin films for reflective and anti-reflective coatings, electronic devices use it for integrated circuits and it is also used for the purification of metals. Dye-sensitised solar cells, insulators, conductors, semi-

conductors, thin film batteries, packaging [30], and in some cases contemporary art, such as the work of Larry Bell [18], have all implemented either thin films or nanostructures. An array of deposition techniques have been utilised over time to achieve the growth of electrical and optical thin films. The performance of the depository substance is determined by the nanostructure formation. Chen *et al.* [12] demonstrates this concept via the used of nickel oxide thin films, whereby the structural features highly influence the electrochromic properties of the film. Different deposition techniques are used according to the substance being deposited and the properties of the end product. There are two foremost categories that each deposition technique is sorted into; this is physical deposition and chemical deposition. Some techniques can be a combination of the two [26; 30; 57]. The Flowchart in figure 2.4-1 shown below gives a brief overview of the different deposition techniques.

The chemical deposition techniques consist of plating (electroplating, chemical solution deposition (CSD)) and chemical vapour deposition (Metal-Organic Chemical Vapour Deposition (MOCVD), plasma enhanced chemical vapour deposition (PECVD)). Chemical deposition works by triggering a chemical change, such as pyrolysis or reduction, in the material [26]. Chemical vapour deposition is the main class of chemical deposition. This method involves chemical reaction between a gas and a volatile material for the film formation. The gas decomposes due to the high temperature they are heated to leading to deposition of a non-volatile solid film. This technique generally deposits particles in a conformational simulation rather than a directional one as the physical deposition does [26].

The physical deposition techniques can also be classed as physical vapour deposition (PVD) techniques as they all are derivatives of it. The PVD techniques include cathodic

arc deposition (arc-PVD), sputtering (Plasma enhanced deposition (PED)), pulsed laser deposition (PLD), and ion beam (gas cluster ion-beam technology (GCIB)).

Molecular beam epitaxy and reactive sputtering are the techniques that use a combination of both physical and chemical deposition [28; 31]. PVD produces thin films of liquids or solids via mechanical or thermodynamic processes to facilitate atomic transfer. The material is vaporised and thereafter transported to a vacuum/low pressure surrounding to condense. The vacuum deposition chamber allows freedom of particle movement. The particles are generally deposited in a directional simulation.

The three main classes in which the techniques below are grouped include evaporation, sputtering and ion beam [30; 57]. PVD does not use any chemical reactions in storing the high energies required. The physical deposition technique of Pulsed Laser Deposition (PLD) will be the main focus in this thesis. A detailed analysis of this technique is given in section 2.4.1 below.

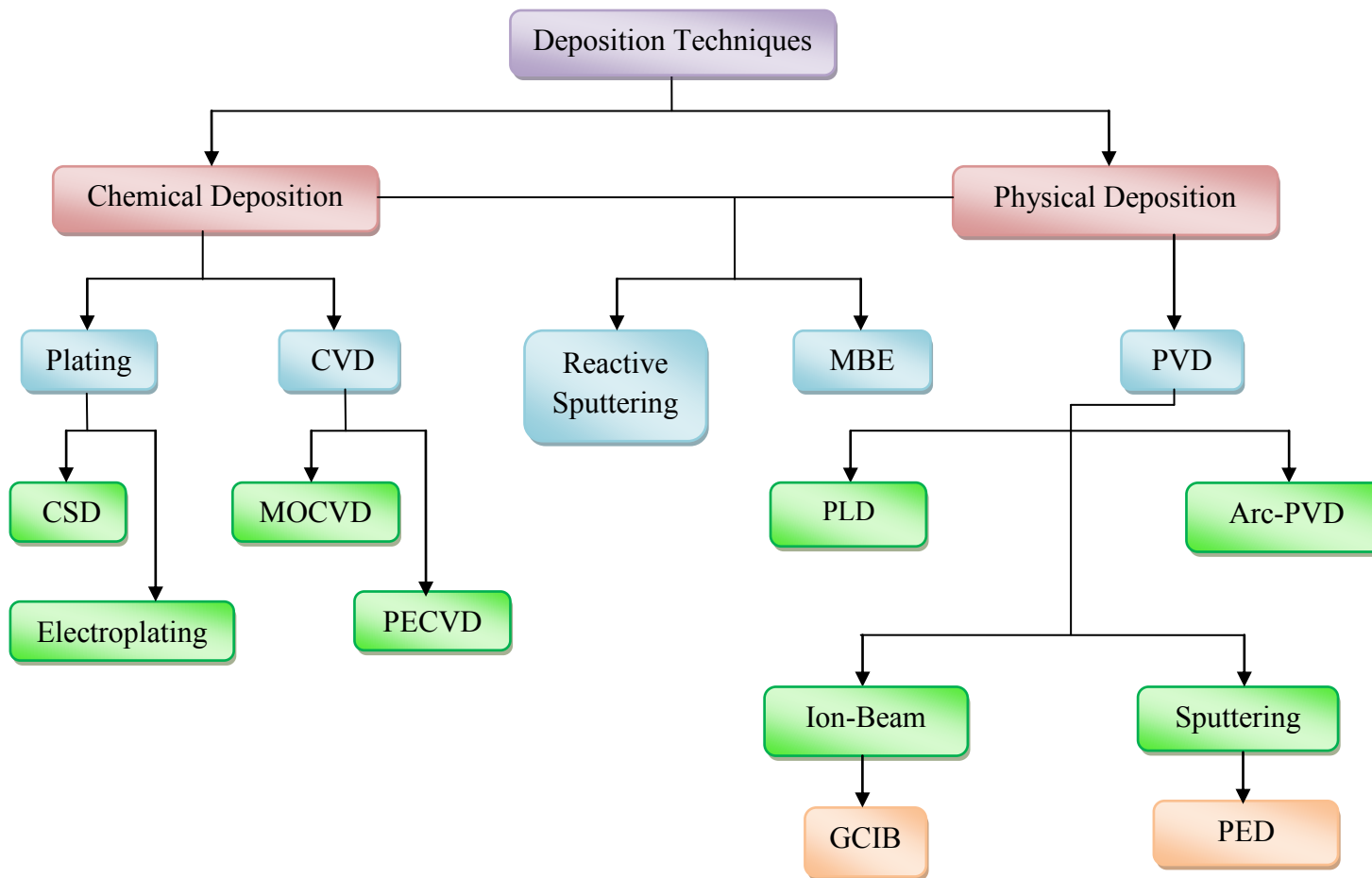


**Figure 2.4-1.** Flowchart showing the classes of deposition techniques. CSD - chemical solution deposition, CVD - chemical vapour deposition, MOCVD - Metal-Organic Chemical Vapour Deposition, PECVD - plasma enhanced chemical vapour deposition, MBE - Molecular beam epitaxy, PVD - physical vapour deposition, PLD - pulsed laser deposition, arc-PVD - cathodic arc vapour deposition, GCIB - gas cluster ion-beam technology, PED - Plasma enhanced deposition.

### **2.4.1. Pulsed laser Deposition (PLD)**

Pulsed laser deposition is proficient at producing complex chemical compounds such as multicomponent thin-film materials for conductors, insulators, semiconductors as well as biological materials [21]. The operational principles of a PLD system utilise a laser source (with pulses of approximately 300nJ/pulse) to irradiate a target [57]. These pulses are short with a high energy density resulting in high absorption by the target [21]. The procedure is carried out in a vacuum whereby the target absorbs the laser energy followed by ionization and electronic excitation of the energy (dense targets are used for ceramics). The laser wavelength and refractive index of the material have to be taken into account; a short wavelength laser that operates in UV light is used for ceramics [21]. This energy is then changed into thermal and mechanical energy to cause ablation and evaporation and thus forming a plasma plume containing ions, electrons and atoms [17]. These free particles of the plume oscillate with the laser's electromagnetic field. The ablation plume provides the material flux needed for growth of the film consequently the plume particles are transferred towards the hot substrate surface. Collision of these particles causes the energy to be transferred to the substrate surface where it is heated to vaporise the material. This then causes anisotropic adiabatic expansion of the plume. The pressure inside the PLD chamber determines the distribution. Reflection high energy electron diffraction (RHEED) is combined nowadays to achieve the monolayer by monolayer growth [21].

With each laser pulse material is evaporated. The deposited energy on the target is equal to the required vaporization energy, substrate conduction loss as well as plasma absorption loss. The film growth occurs when there is a thermal equilibrium. The features affecting the film growth per laser pulse includes the:

- ◆ Laser wavelength
- ◆ Laser energy density
- ◆ Laser spot size
- ◆ Substrate surface and temperature
- ◆ Pressure
- ◆ Target-substrate separation

When controlling the film stoichiometry during deposition, the laser energy is of crucial importance [83]. The oxygen partial pressure inside the PLD chamber determines the distribution, size and shape of the forming nanostructures. The number of pulses affects the volume of the deposited material which in turn affects the nanostructure shape [76].

Figure 2.4.1-1(a) and (b) show an image of a Neocera Cluster II PLD system and diagrammatic representation of a PLD system respectively.

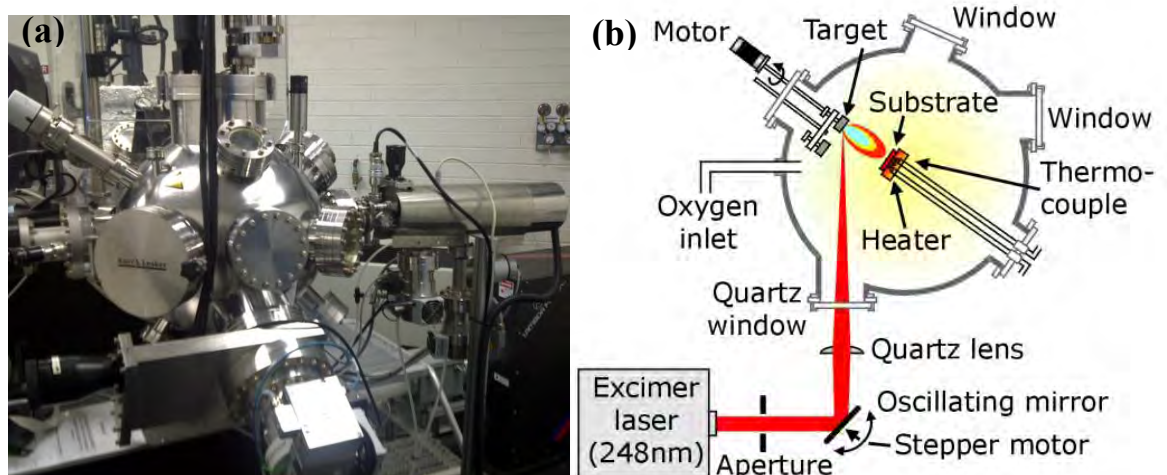


**Figure 2.3.1-1** (a) Neocera Cluster II PLD system (b) a diagrammatic representation of a PLD system [54].

A Neocera Cluster II PLD system was used in this thesis. It consists of a:

- ♦ Lambda Physik 248 nm krypton fluoride (KrF) exclaimer laser
- ♦ Vacuum chamber
- ♦ Substrate heater
- ♦ Pfeiffer turbo pump and pressure gauge
- ♦ Motorised target holder

PLD demonstrates that the synthesized materials crystalline state, growth rate and stoichiometry can be accurately controlled along with the ability to grow inorganic epitaxial multication thin films [21]. Bonding between the deposited material and the substrate surface is also very strong. The appropriate phase formation of the oxide is made possible via the growth flux with correct stoichiometry in an oxidising environment. Target stoichiometry is shown to be reproducible as confirmed by the synthesis of complex multication oxide crystals by PLD; this being an advantage over most of the other techniques [21].

Depositing patterns onto a substrate is also possible by using the laser to vaporise material from a film on transparent material to a substrate facing the film. This entails vaporising a controlled film area [9]. This technique can also be used to synthesise optical NiO films for use as sensors in gas detection devices [22]. Khakani used PLD to deposit nanostructured tin oxide films on alumina substrates for the purpose of gas sensors. PLD applications are expected to obtain a high value end product with low volumes [31]. Synthesis of manganite composition thin films by Hwang *et al.* [38] shows that in reducing growth conditions high quality atomically flat surfaces are possible as well as a superior phase stability in the presence of stoichiometric cation delivery.

## 2.5. Characterisation Techniques

In this thesis a number of characterization approaches were employed. This chapter elucidates on these approaches. From the mid 1800's when microstructure analysis was developed [6], there has been significant enhancements toward new material developments. Since then different analysis techniques have been exploited to assist in understanding microstructural and nanostructural components in relation to their properties (mechanical, thermal, electrical, optical, magnetic, *etc.*) and how they can effectively be harnessed in applications. These micro- or nanostructured components are a reflection of the processing conditions. Through characterisation the structural evolutions can be distinguished as well as the compositions.

Continuous enhancements of sample preparation and products have been an offshoot of microstructural analysis [6]. Today characterisation tools are well established in nano- and microscale characterisation and development of complex materials and processes as well as intricate structures. Each of the tools, mentioned below, may be used for analysing metal oxide nanostructures either internally or externally. These tools allow the specimen or specimens' internal structure to be clarified by magnification as well as establishing the internal component interactions. This has been taken advantage of in the petroleum industry, solid state devices, aerospace, automotive components and ceramics [6]. Visualisation of specific materials at nano-, micro-, macro- resolution levels, was performed using a SEM to observe the morphology, an AFM to analyse the dimensional aspects of the morphology and a TEM to analyse the morphology at high magnification. Elemental analysis (composition and arrangement of atoms) was then performed using EDS and XRD. Functional properties were investigated using

conductive-AFM. These methods are now particularly discussed below in context to their application for this thesis.

### **2.5.1. Atomic Force Microscopy (AFM)**

A Veeco Digital Instruments Multimode SPM and a JEOL JSPM 5400 MkII Environmental AFM was used for analysis of the NiO nanostructures. The AFM is particularly useful in visualising thin-film growth morphology and grain size. It is one of the main instruments used for manipulating metal oxide matter at the nanoscale. In air the AFM has a resolution of 30 Ångstroms horizontally and less than 1 Ångstrom vertically [5].

The AFM has been valuable in providing information on nanostructures, particularly NiO nanostructures in our case. This is also exemplified by Hsu *et al.* who use the AFM as a major component in the fabrication of NiO nanostructures [35]. Depending of the type of tip, the AFM can be used to measure many interaction forces between the probe tip and the surface of interest. For example the electrostatic forces can be measured when the probe tip is a small diamond, carbon nanotube or silicon chip. Thermal conductivity is measured when the tips resistance changes with temperature. Magnetic forces are measured when the tip is sensitive to magnetic fields. Frictional forces are measured when the probe is dragged across the sample surface [86]. The AFM is useful in analysing the microscopic events at the same scale of occurrence [67]. The AFM can obtain structural images via two basic modes. Contact mode is where the tip applies larger lateral forces to maintain contact with the surface as it moves in the x – y directions. Tapping mode is where the tip intermittently contacts the sample surface. No lateral forces are applied to the sample [32].

Conductive- AFM (C- AFM) allows for electrical characterisation of nanometric areas to be made via the use of a conductive tip. This makes it possible to measure electrical properties of nanostructures that are not possible through macroscopic instrumentation. This is shown in literature [67] as the degradation process of ultrathin SiO<sub>2</sub> films in metal oxide semiconductor structures are examined. C- AFM is one of the key techniques used in this study to investigate the resistive switching properties.

### **2.5.2. X-Ray Diffraction (XRD)**

X-ray diffraction (XRD) is a non-destructive method that allows the crystallographic structure (arrangement of atoms in a structure) and chemical phase composition to be determined. XRD was one of the more significant tools used in the characterisation of NiO nanostructures. The data obtained from this instrument has allowed for lattice calculations, phases present, contamination, etc. to be made and therefore is discussed in more detail.

XRD works by focusing a beam through a sample; the beams scatter and land on a detector to form a diffraction pattern. The beam strengths are collected as the crystal is rotated allowing for the bond strength and oscillation of the crystal can be determined. Generally a monochromatic x-ray source found in the range of 0.5 – 2.5 Å is needed for x-ray diffraction [19]; for that reason the K $\alpha$  radiation is isolated from the neighbouring radiation wavelengths.

Diffraction is the phenomenon of scattering. The diffracted beam consists of rays scattered by the successive atomic planes comprised within the crystal. As these x-rays are diffracted off the arrangement of atoms (crystal lattice) in the crystal, interference

patterns are formed. The size and shape of the unit cell determines the diffraction directions and the positions of the atoms in the unit cell determine the intensity [19]. The resultant intensity is portrayed as sharp peaks with identical symmetry to that of the atoms dispersed within meaning that the atomic distance directly equates to the diffraction pattern formed. This therefore makes XRD ideal for determining the distribution of atoms in a material. XRD is a non-destructive method that allows a determination of the crystallographic structure (arrangement of atoms in a structure) and chemical phase composition to be made. The XRD pattern of a pure substance is unique as stated by Hull [37] “...every crystalline substance gives a pattern; the same substance always gives the same pattern; and in a mixture of substances each produces its pattern independently of the others”.

The diffraction relationship between the reflections and incidence angles of the x-ray beams upon striking a crystal surface were discovered by W.H Bragg and W.L Bragg. Their theory is known as Bragg’s Law, this is shown in equation 2.5.2-1 where Bragg’s law describes that the reflection from a crystal lattice states the crystal lattice conditions for interference from the successive planes ( $h, k, l$ ).

$$2d\sin\theta = n\lambda \quad 1$$

*Equation 2.5.2 -1. Bragg’s condition. Where  $n$  is the order of reflection (integer),  $\lambda$  is the wavelength,  $d$  is the distance between crystal planes and  $\theta$  angle observed at a diffraction peak [34].*

XRD shows the interaction between the three dimensional atomic layers in a material (crystal lattice). These atoms have a parallel arrangement, with a distance,  $d$ , between

them. The distance varies depending on the material in question. Depending on the Bravais lattice structures, the d spacing values can be calculated.

Natural and manufactured materials from a range of research fields require the use of XRD to provide information on applications. XRD is a non-destructive method that allows the crystallographic structure (arrangement of atoms in a structure) and chemical composition to be determined. XRD can therefore be used to investigate thin film phases, crystal structure, lattice parameters, residual stress, epitaxial or polycrystalline structures, reciprocal space mapping as well as spacing in crystallites such as polymer stacking and particle size distributions [10; 19; 60]. An example of where XRD has been used is in the sonochemical characterisation of nanometre-sized transition metal oxides, such as iron, nickel, cobalt, copper, and zinc (synthesised from metal acetates) [46]. The XRD measurements allowed a comparison to be made of the samples that used water as a solvent during synthesis and those that did not.

### **2.5.3. Scanning Electron Microscopy (SEM)**

A Fei Nova SEM230 is used for analysis. The SEM is one of the most promising instruments used for examination and analysis of microstructural properties of objects. It allows a determination of the crystal structure and grain orientation of the metal oxide of interest to be made. The 3 dimensional images produced are of very high resolution with details showing at less than 1 nm [29]. Properties such as surface topography, composition and conductivity can be inferred from the SEM.

The SEM forms the basis for microstructural characterisation in many forms of research especially in characterising metal oxide nanostructures. Literature shows how fabricated

metal oxide thin films and coatings are analysed via SEM [82]. Vayssieres fabricates ZnO nanowires and monitors the growth using the SEM, which allows surface morphology and orientations to be controlled. Using the SEM in the highest possible resolution mode it is possible to infer what our individual NiO nanostructures look like.

The SEM also has the ability to carry out elemental analysis on samples by using characteristic x-rays. The techniques that perform this function are energy dispersive x-ray spectroscopy (EDS) and wavelength dispersive x-ray spectroscopy (WDS). During the analysis of NiO just the EDS is sufficient in providing the needed information.

## **I. Energy Dispersive Spectroscopy (EDS)**

EDS is a technique utilising the excitation of x-ray to detect the elemental components of a sample [29]. EDS has become a leading method for x-ray microanalysis in the SEM. It presents a way of accurately performing a quantitative analysis of a samples major elemental constituent (>10 wt%) [29]. This technique is used for the elemental analysis of the NiO deposited onto the STO substrate to determine the percentage of each element and if there are any contaminant traces, of bismuth for example (which may not have evaporated during step two of the deposition). Vayssieres [82] also uses the EDS component of the SEM to confirm that the aqueous chemical growth of the ZnO obtained has Zn and O without any C or N contamination.

### **2.5.4. Transmission Electron Microscopy (TEM)**

The TEM can be used to obtain information of the crystal orientation, electronic structure, chemical identity and electron phase shift. It is well suited to observing

nanoscale metal oxide materials in 1D, 2D and 3D. The image contrast will depend on the absorption of electrons, which is influenced by thickness and composition of the material. Beam energies ranging from 100 000 to 400 000 eV are used [88]. The TEM can magnify up to 500 000 x magnification. Choi *et al.* [16] utilise the TEM to determine the existence of Ge nanocrystals in a metal oxide layer (SiO<sub>2</sub>). Hence the memory effect of the trilayer structure (rapid thermal oxide / Ge nanocrystals in SiO<sub>2</sub> / sputtered SiO<sub>2</sub>) can be investigated.

## CHAPTER 3. EXPERIMENTAL PROCEDURE

### 3.1. Phase Separation Approach

The nanostructures are deposited, using pulsed laser deposition (PLD), on a STO (001) substrate. Using the phase separation approach [7] it is possible to generate the phase separated constituents of  $\text{Bi}_2\text{O}_3$  and NiO from the bismuth nickel oxide (BNO) perovskite precursor. This approach consists of two steps [7] as seen in Figure 3.1-1. Step one, shown in Figure 3.1-1(a) is to create an environment to promote perovskite instability (in this case it is depositing with a substrate temperature of 900 °C and pressure of 50 mTorr) hence forming the  $\text{Bi}_2\text{O}_3$  and NiO island matrix. Separation of the BNO occurs due to the metastable state of the BNO. The bismuth and nickel react with the oxygen atoms to form  $\text{Bi}_2\text{O}_3$  and NiO.

Step two in Figure 3.1-1(b) shows the removal of the  $\text{Bi}_2\text{O}_3$  via evaporation in a high vacuum environment. The high volatility and thermodynamic instability of bismuth  $\text{Bi}_2\text{O}_3$  is exploited and an irreversible decomposition of the sample occurs, allowing epitaxial (monocrystalline) structures to form. This leaves behind the required self assembled NiO nanostructures. Then a further annealing step is shown to promote crystallisation and phase formation of the nanostructures (carried out at 900 °C in a partial oxygen environment of 1 Torr).

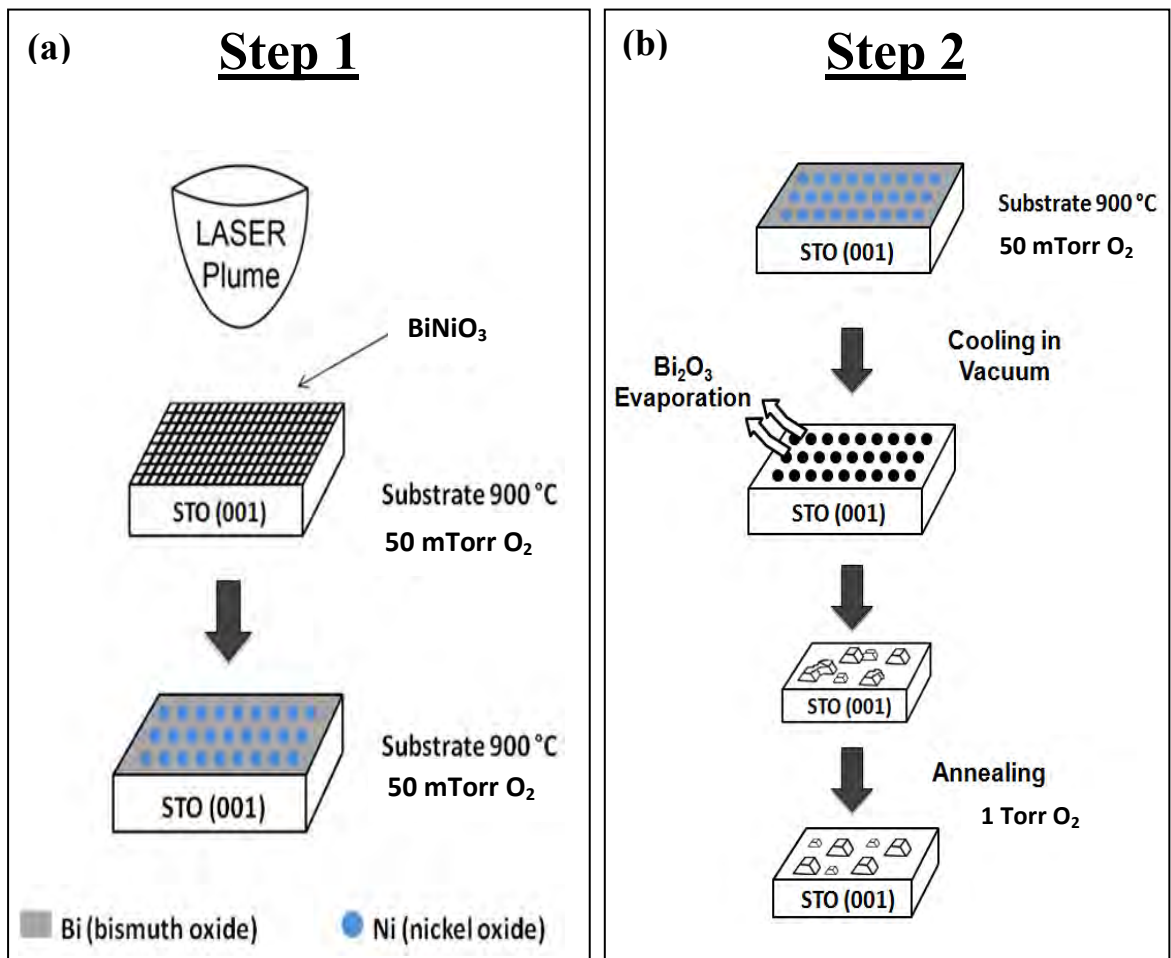


**Figure 3.1 -1.** Schematic representation of the phase separation approach [7].

(a) Step 1: Synthesis approach (b) Step 2: Bismuth oxide removal.

### 3.2. Reflection High Energy Electron Diffraction (RHEED) analysis

To verify our results using the phase separation approach, RHEED analysis was conducted during the deposition process. Measurements were carried out using a RHEED-electron gun in transmission mode with a primary energy of 20 keV. Measurements taken correspond to the diffraction patterns taken with a TEM.

This method allows the crystallographic data of sample surface to be obtained. Figure 3.2-1 shows this RHEED analysis conducted during a deposition. A clean, flat STO

surface is indicated by the reflections of the Laue circles. This is formed due to the interference between diffracted electrons. The before deposition image in Figure 3.2-1(a) shows this clean substrate surface. Immediately after the deposition another image was taken; Figure 3.2-1(b) shows a weak NiO(200) diffraction pattern when compared to a known NiO(200) electron diffraction pattern obtained from Webemaps [97] (Figure 3.2-1(d)). Here we see that the surface is no longer flat and the Bi has completely volatilized. Figure 3.2-1(c) show this diffraction pattern becoming more prominent after the cooling down process.

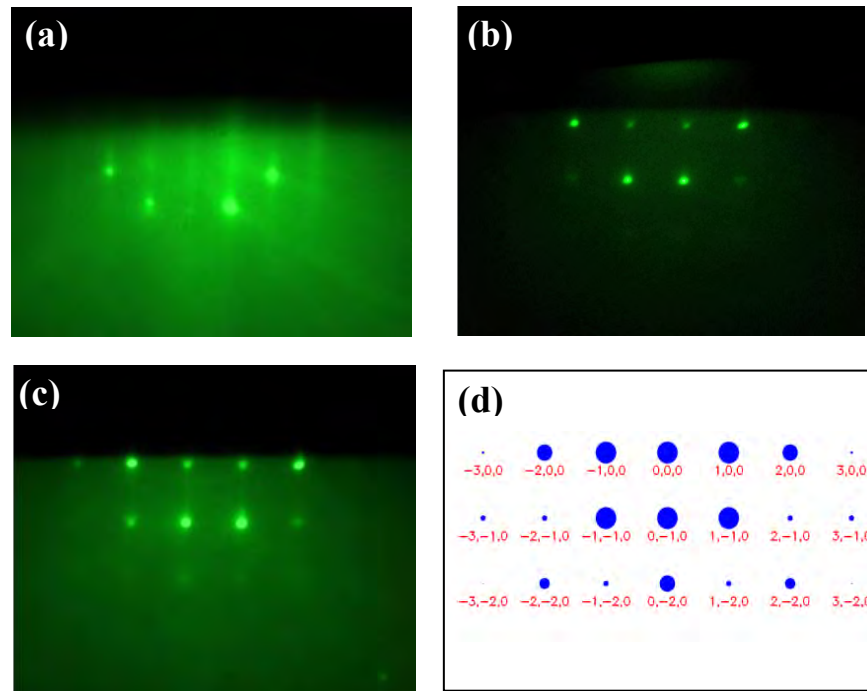


**Figure 3.2 -1.** RHEED pattern for (a) blank STO – before deposition (b) NiO after deposition (c) NiO after cooling down (d) corresponding diffraction pattern taken from Webemaps [97].

### **3.3. Sample Preparation**

#### **3.3.1. Synthesis Method**

##### **I. Pulsed Laser Deposition (PLD)**

As mentioned earlier a Neocera Cluster II PLD system was utilised to deposit NiO nanostructured samples.

*The materials used include:*

- ◆ A bismuth Nickel Oxide, BiNiO<sub>3</sub> (BNO) target
- ◆ Substrates including strontium titanate (SrTiO<sub>3</sub> or STO) in (001), (110), (111) orientation and Nb:STO in (001) orientation (0.05% Nb doped STO)
- ◆ A diamond tip cutter
- ◆ P320 and P600 sand paper
- ◆ A hotplate heater
- ◆ Isopropanol
- ◆ N<sub>2</sub> gas
- ◆ Conductive silver paint

##### **A. Deposition**

A diamond cutter is used to cut a piece of substrate (STO) to ~ 5 mm × 5 mm dimensions which is then added to a beaker filled with isopropanol and placed into the sonicator for 2 minutes for cleaning purposes. The substrate holder and BNO target is then sanded and the substrate holder wiped with acetone. The substrate is then dried using nitrogen gas and adhered to the substrate holder using conductive silver paint.

Bonding is enforced and solvent evaporated by heating the substrate holder and substrate for approximately 30 seconds on the hotplate. The substrate holder and target is loaded into the PLD chamber whereby the entry points are wiped down with methanol to remove any cross contamination factors.

The chamber pressure is allowed to reach  $\sim 6 \times 10^{-6}$  Torr using the turbo pump followed by substrate heating to 900 °C (or desired temperature). The pressure is then adjusted to 50 mTorr (or desired pressure) by adjusting the turbo speed and opening the oxygen gas valves. The KrF laser is then turned on and the target motors are then utilised to rotate the BNO target at 57 °/minute and raster at  $\pm 12^\circ$  to allow an even spread of material during deposition. The shutter mask must be closed before pre-ablation. Pre-ablation is carried out by firing 2 000 pulses at 10 Hz. The shutter mask is then opened and deposition is commenced by firing 5 000 pulses at 5 Hz (or desired number of pulses and frequency). The pressure must be maintained during this time by altering the turbo speed.

When the laser ablation has ceased, the gas valves are closed, turbo speed restored to operating speed, rotation and rastering is stopped, laser is turned off and the substrate is allowed to cool to room temperature at 3 °/minute (or desired cooling rate). Once cooled, the chamber can then be purged with nitrogen gas for sample removal. The various deposition parameters are summarised in table 4.1-1 in the results and discussion section.

## **B. Post Deposition Annealing**

Similarly to depositing the substrate holder is sanded and wiped with acetone. The substrate is then adhered to the substrate holder using conductive silver paint. Bonding is enforced by heating the substrate holder and substrate for approximately 30 seconds. The substrate holder is loaded into the PLD chamber.

The chamber pressure is allowed to reach  $3 \times 10^{-6}$  Torr using the turbo pump followed by substrate heating to 900 °C (or desired temperature) at 20 °/minute. The pressure is then adjusted to 1 Torr (or desired pressure) by adjusting the turbo speed and opening the oxygen gas valves. This is then held for duration of 2 hours (or desired time). After which the substrate is allowed to cool to room temperature at 20 °/minute (or desired cooling rate). Once cooled, the chamber can then be purged with nitrogen gas for sample removal as with depositing. The various annealing parameters are summarised in table 4.1-1 in the results and discussion section.

### **3.3.2. Characterisation Preparation**

#### **I. AFM**

For obtaining an image the sample is mounted onto an aluminium stub for the Multimode SPM or a gold plated stub for the JEOL JSPM using double sided copper tape. The stub is then mounted onto the AFM stage followed by mounting of the tapping mode AFM tip and the cover closed. The tip used is an OTESPA/Bruker Si tip. Alignment of the laser is then carried out followed by tuning of the AFM tip. The topography AC-tapping mode is then selected. The AFM is then ready for imaging. The

area size is selected (usually 1  $\mu\text{m}$  or 500 nm) and the scan speed is set to  $\sim 3 \mu\text{m}/\text{sec}$  to  $\sim 6 \mu\text{m}/\text{sec}$  depending on the clarity of the image. Pressing the 'play' button allows an image to be taken.

To obtain I-V measurements a sample is first mounted onto a gold plated stub for the JEOL JSPM 5400 using conductive silver paint. The stub is then mounted onto the AFM stage along with the contact mode AFM tip. Pt-Ir tips were used to apply a sample bias. The cover is then closed to prevent any contamination and alignment of the laser is then carried out. The mode selected is contact mode. The AFM is then ready for use. Firstly an image is acquired whereby the mode is changed to spm in the settings tab and the change input signal to current signal (Lin) is selected from the I-V tab. The bias (in bias tab) is set to 'sample'. Next the I-V points are positioned on the image where measurements are to be taken. Pressing the 'play' button allows a measurement/s to be taken.

## **II. XRD**

The sample is adhered to a glass slide using double sided tape and mounted onto the sample stage. Before analysis the soller slits ( $0.04^\circ$  rad), divergent slits ( $1/4^\circ$  or  $1/8^\circ$ ) and Cu /Ni 0.2 mm attenuator must be in place. The sample is aligned for 2-theta, Z, and omega. The Ni 0.2 mm attenuator then replaces the Cu /Ni 0.2 mm attenuator. The sample is then scanned from a 2-theta of  $0^\circ$  to  $90^\circ$ .

### **III. SEM**

The sample is mounted onto an aluminium stub using double sided copper tape. The chamber of the SEM is vented and the stub is mounted accordingly. The chamber is then allowed to reach a certain pressure before the beam can be turned on and imaging may commence. An accelerating voltage of 2 – 4 kV is used along with a spot size of approximately 2.5 – 4 mm. The working distance is set to 5 mm and the through lens detector is selected for high powered imaging.

#### **A. EDS**

Similarly to setting up for SEM imaging, a sample is mounted onto an aluminium stub using double sided copper tape. The chamber of the SEM is vented and the stub is mounted accordingly. The chamber is then allowed to reach a certain pressure before the beam can be turned on and imaging may commence. An accelerating voltage of 15 kV is used along with a spot size of approximately 5 mm. The working distance is set to 8 mm and the CCD camera is turned off. An area is selected for analysis via x-ray.

### **IV. TEM**

TEM studies were carried out by Ms. Xuan Chen at the University of Sydney and A/Prof Valanoor at Queens University, Belfast. Samples were prepared by both, focused ion beam milling (FIB) and tripod polishing. The high resolution images were taken using a JEOL 3000F at the University of Sydney. Diffraction patterns were acquired on a Philips CM200 at UNSW and JEOL XYZ at Queens University, Belfast.

## **CHAPTER 4. RESULTS AND DISCUSSION**

### **(SYNTHESIS OF NICKEL OXIDE NANOSTRUCTURES)**

#### **4.1. Understanding the role of synthesis parameters**

NiO nanostructures deposited via PLD using the phase separation method as explained earlier have been analysed and distinguished according to the conditions used during synthesis. The analysis of the experiments carried is focused on the effects of varying the:

- ◆ Chamber O<sub>2</sub> partial pressure during deposition
- ◆ Temperature during deposition
- ◆ Number of laser pulses during deposition
- ◆ Chamber O<sub>2</sub> partial pressure during annealing

A determination of the most favourable conditions in optimising NiO nanostructures can then be made. Therefore the sample should be phase pure with no contamination (e.g. Bismuth) as well as form into discrete nanostructures with a minimal interfacial energy and highest planar density for a FCC cubic structure [44; 79]; this would be square pyramidal shaped nanostructures [55]. Each of these effects is discussed in more detail below. The conditions that were experimented with are summarised in table 4.1-1.

**Table 4.1-1. Deposition and Annealing Conditions (all samples were annealed for 2 hours).**

<b>Substrate Temp (°C)</b>	<b>O<sub>2</sub> Pressure (mTorr)</b>	<b>No. Of Pulses</b>	<b>Cooling Rate (°C/min)</b>	<b>Annealing Pressure × 1</b>	<b>Annealing Pressure × 2</b>
860	10	5 000	3 in vac	1 Torr	N/A
	35	10 000	5 in vac	vacuum	N/A
		5 000	3 in vac	100 mTorr	1 Torr
	50	5 000	3 in vac	100 mTorr	1 Torr
	100	5 000	3 in vac	1 Torr	N/A
		10 000	5 in vac	vacuum	N/A
900	50	5 000	3 in vac	1 Torr	N/A
		10 000	3 in vac	1 Torr	N/A
		20 000	3 in vac	1 Torr	N/A

#### 4.1.1. Varying the Deposition Pressure

The first part of the investigation was to vary the oxygen partial pressure. The oxygen pressure has an influence on the shape and chemistry of the plume and therefore on the morphology of the nanostructures. Samples were deposited at 10, 35, 50 and 100 mTorr with the temperature, number of pulses, cooling rate and annealing pressure kept constant at 860 °C, 5 000 pulses, 3 °/minute and 1 Torr respectively. Figures 4.1.1-1 to 4.1.1-4 illustrates the differences in each condition.

The sample shown in figure 4.1.1-1 was deposited onto STO (001) at a temperature of 860 °C, an O<sub>2</sub> pressure of 10 mTorr, with 5 000 pulses, cooled at 3 °/min in a vacuum and then annealed for 2 hours at 900 °C in 1 Torr O<sub>2</sub>. Observations from the SEM image in Figure 4.1.1-1(a) display a maze-like structure where the nanostructures are still joined. This implies that the conditions were not sufficient in allowing the separation of individual nanostructures. The same maze like structure is displayed by the AFM image in Figure 4.1.1-1(c) which corresponds to the SEM. Analysis via the AFM tells us that these networks of structures range from approximately 13-48 nm in height. From the XRD in figure 4.1.1-1(b) we see only (001) reflections from the STO (refer to appendix A) and NiO, which reveals that the sample is epitaxial (JCPDS 01-071-1179). Appendix B shows the reflections from the substrate holder. The NiO (200) peak is evident at  $2\theta = 43.465$ . The out-of-plane lattice parameter, 4.159 Å, is much lower than that of the bulk (4.178 Å). Complete vaporisation of the bismuth is confirmed with no Bismuth related peaks. The EDS image shown in figure 4.1.1-1(d) was taken using a SEM. It also verifies that there are no elemental traces of bismuth (no bismuth peak) in the sample. Only the intended Ni, Sr, Ti and O peaks are evident.

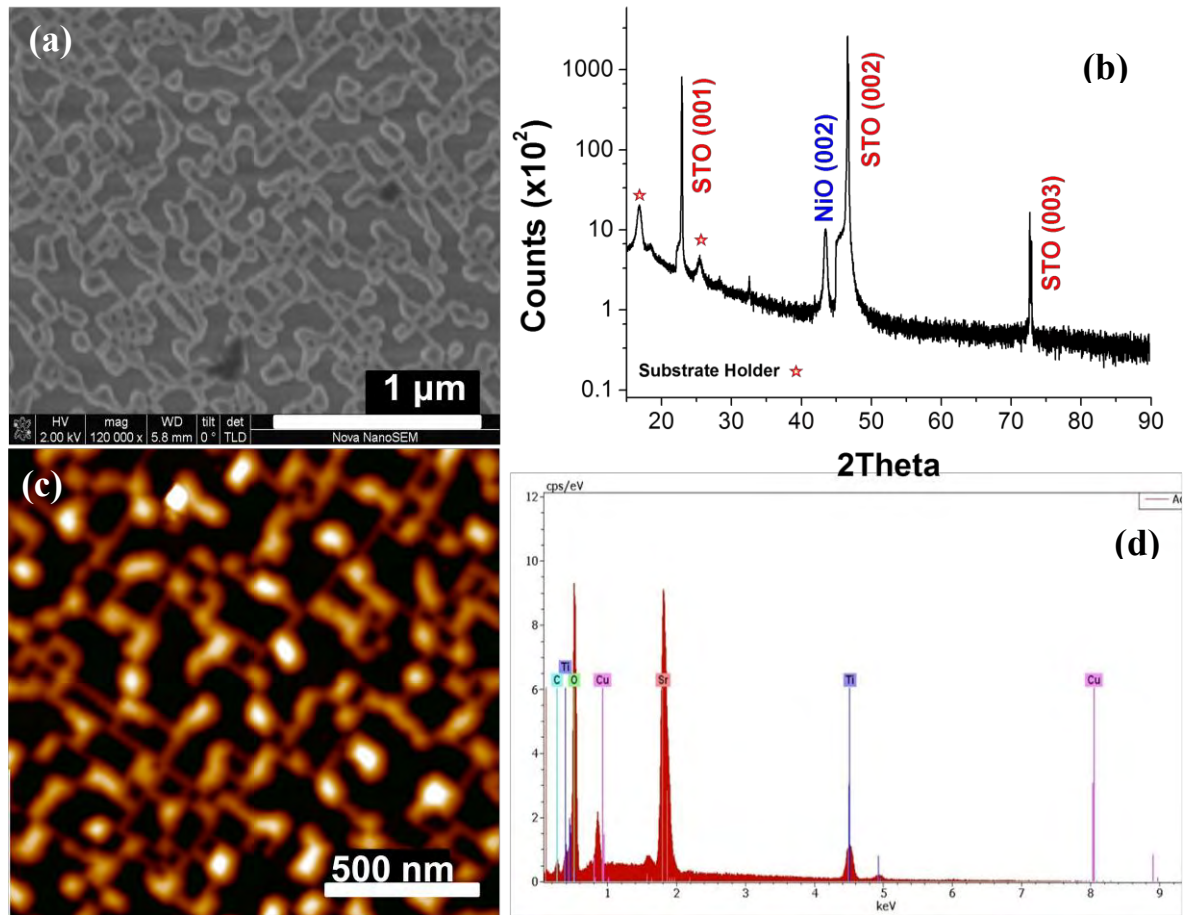


*Figure 4.1.1 -1. Sample images for depositing in 10 mTorr O<sub>2</sub>, 5 000 pulses, 860 °C and annealing in 1 Torr O<sub>2</sub> on STO (001) (a) SEM (b) XRD pattern (c) AFM (d) EDS.*

The next sample shown in figure 4.1.1-2 was deposited onto STO (001) at a temperature of 860 °C, an O<sub>2</sub> pressure of 35 mTorr, with 5 000 pulses, cooled at 3 °/min in a vacuum and then annealed for 2 hours at 900 °C in 1 Torr O<sub>2</sub>. Unlike the sample shown in figure 4.1.1-1, we can see a significant change by the formation of discrete nanostructures.

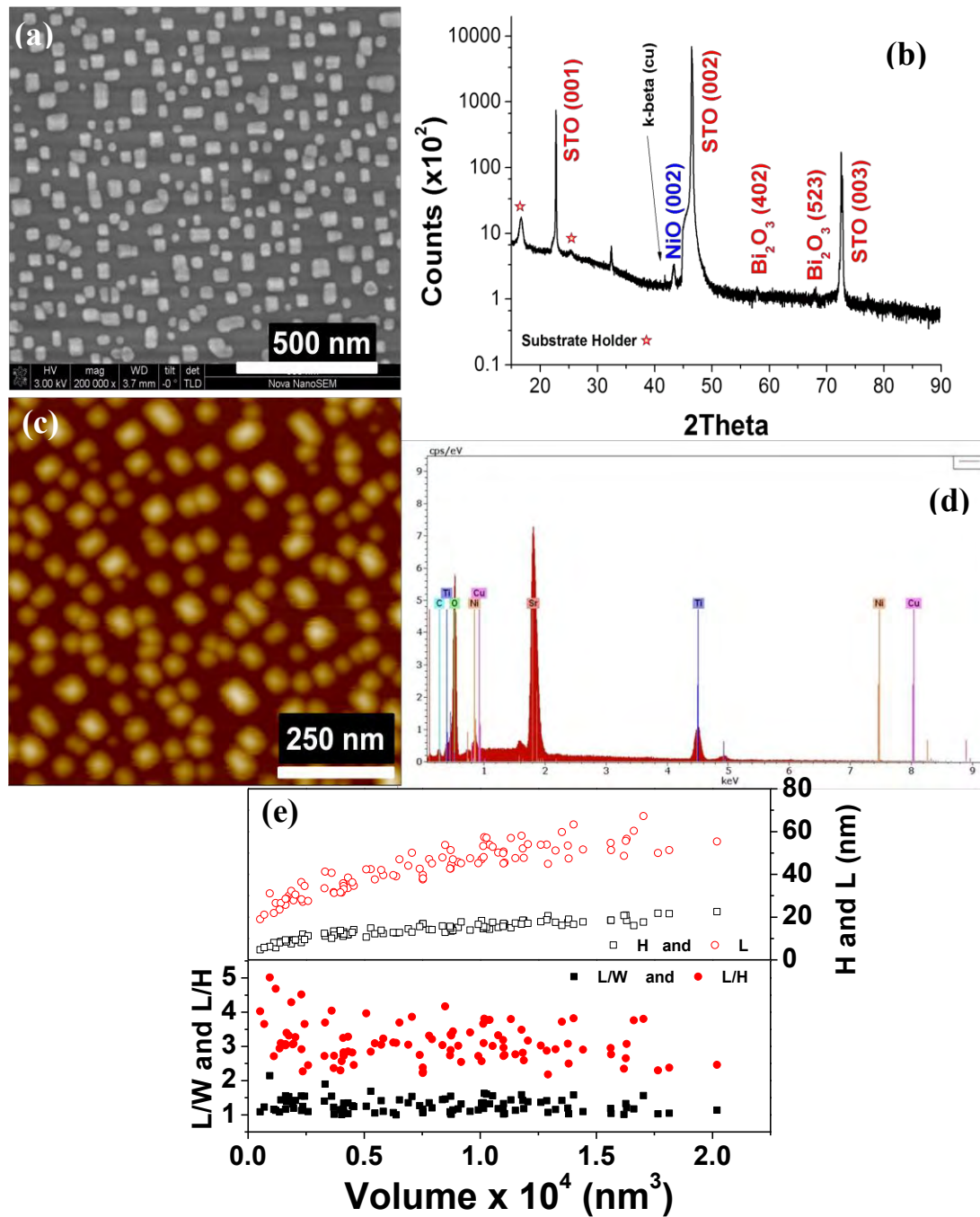


*Figure 4.1.1 -2. Sample images for depositing in 35 mTorr O<sub>2</sub>, 5 000 pulses, 860 °C and annealing in 1 Torr O<sub>2</sub> on STO (001) (a) SEM (b) XRD pattern (c) AFM (d) EDS using SEM (e) Measured Length(L)/Width(W) ratio (black filled square), L/Height(H) ratio (Red filled square), H (black open square) and L (red open square) as a function of nanostructure volume.*

By changing the deposition  $O_2$  pressure to 35 mTorr we see a selection of square pyramidal shaped structures as portrayed in the SEM image in figure 4.1.1-2(a). From this image we can also see that some of these structures have not completely separated. To further support these observations we may also refer to the AFM image in figure 4.1.1-2(c). By examining the dimensions (height (H), width (W) and length (L)) of these nanostructures we were able to construct the size analysis plot as a function of the nanostructure volume (figure 4.1.1-2(e)). This plot was obtained by calculating the volume of each nanostructure using the volume of a pyramid ( $1/3 LWH$ ). The L, H, L/H and L/W were then plotted as a function of volume. The range of heights is found to be from 5-25 nm tall. This plot shows a volume coarsening transition as the H and L increase [55]. The L/H ratio is seen to be independent of volume with a range from 2-5. The L/W ratio (surface area) ranges from 1-2. This shows that both square and rectangle pyramidal shaped structures are found with increasing volume. This is implying that an equilibrium shape has not yet been achieved. Although 35 mTorr gives us formations of individual nanostructures we see that it does not suffice in completing the phase separation approach as seen from the XRD in figure 4.1.1-2(b) where the NiO(200) peak at  $2\theta=43.437$  is evident but so are  $Bi_2O_3$  (402) and  $Bi_2O_3$  (523) peaks. Calculation of the lattice parameter gives 4.162 Å, which is lower than that of the bulk at 4.178 Å. In determining the elemental composition of the sample EDS was carried out (figure 4.1.1-2(d)). From this we see Ni, Sr, Ti and O peaks as well as a Cu peak from the copper tape used to affix the substrate to stub (holder) however no traces of elemental bismuth are shown meaning that the amount of bismuth would be less than 10 wt %.

The next sample to be discussed (Figure 4.1.1-3) was deposited onto STO (001) at a temperature of 860 °C, an  $O_2$  pressure of 50 mTorr, with 5 000 pulses, cooled at 3 °/min in a vacuum and then annealed for 2 hours at 900 °C in 1 Torr  $O_2$ .

By further increasing the deposition O<sub>2</sub> pressure to 50 mTorr we see (from the SEM image in Figure 4.1.1-3(a) and the AFM image in Figure 4.1.1-3(b)) the topographical similarities shared with that of the 35 mTorr sample. The array of square and rectangle pyramidal shaped structures were also analysed via the procedure mentioned above to construct a size analysis plot as a function of volume (Figure 4.1.1-3(c)). Here we see the H and L show a monotonic increase similar to the 35 mTorr sample, however both the height and length are greater. The height range was revealed to be from 5-34 nm high. For the smaller islands (lower volume) we see that the L/W ratios vary around 1 revealing that the initial shape of islands is rectangular. Beyond a critical volume ( $\sim 5 \times 10^4 \text{ nm}^3$ ) the L/W ratio remains constant at  $\sim 1$  indicating that the structures have reached an equilibrium surface area. Beyond this critical volume the L/H ratio deviates from 3 suggesting that the nanostructure has not reached an equilibrium height.

To further analyse these nanostructures a TEM image was acquired (shown in figure 4.1.1-3(d)) along with its diffraction pattern (shown in Figure 4.1.1-3(e)). The diffraction pattern was obtained along the  $\langle 110 \rangle$  zone axis. By drawing perpendicular lines from each of the nanocrystal surfaces and transferring them to the diffraction pattern we are able to determine the orientation of each facet. This is shown to be (001) for the top, (-1-11) and (111) for the respective side diagonals. Due to the distinct single spots of the diffraction pattern, the epitaxial nature of this sample is revealed. This is also confirmed by the XRD pattern in figure 4.1.1-3(f) where the NiO(200) peak at  $2\theta = 43.327$  is evident. The out-of-plane lattice parameter is shown to be  $4.1716 \text{ \AA}$  which is similar to the 35 mTorr sample. The xrd does not show any bismuth contamination unlike the 35 mTorr sample in figure 4.1.1-2. The Ni, Sr, Ti and O peaks as well as copper (from the copper tape) are seen with no contaminating Bi in the EDS image (Figure 4.1.1-3(g)).

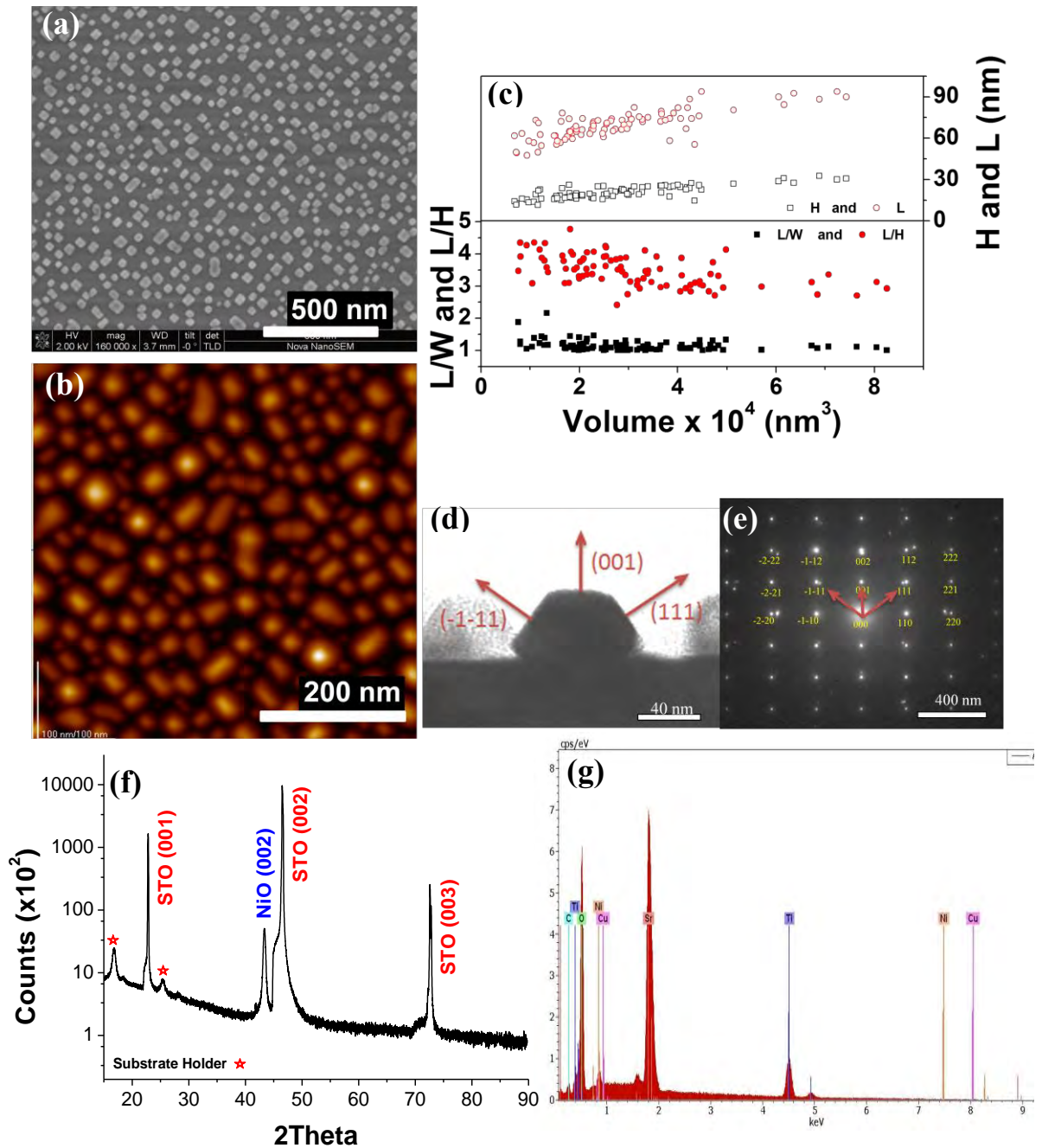


**Figure 4.1.1 -3 .** Sample images for depositing in 50 mTorr  $O_2$ , 5 000 pulses, 860 °C and annealing in 1 Torr  $O_2$  on STO (001) (a) SEM (b) AFM (c) Measured Length(L)/Width(W) ratio (black filled square), L/Height(H) ratio (Red filled square), H (black open square) and L (red open square) as a function of nanostructure volume (d) TEM (e) TEM diffraction pattern (f) XRD pattern (g) EDS using SEM.

Increasing the deposition O<sub>2</sub> pressure (to 100 mTorr) was carried out once more for the last comparison of the pressure variation. Here a sample was deposited onto STO (001) at a temperature of 860 °C, an O<sub>2</sub> pressure of 100 mTorr, with 5 000 pulses, cooled at 3 °/min in a vacuum and then annealed for 2 hours at 900 °C in 1 Torr O<sub>2</sub>. Figure 4.1.1-4 shows this data.

Looking at both the SEM and AFM images in figure 4.1.1-4(a) and (b) respectively, we can see that the inter-particle distance has increased when compared to the 50 mTorr sample in Figure 4.1.1-3. However the nanostructures appear to have slightly rounder edges than its predecessor. This occurs as a result of adatomic diffusion and volume limitations whereby after reaching a maximum shape the atomic diffusion occurs at the edges. Some of the structures also appear to be joining. Using the AFM and hence the constructed size analysis plot in figure 4.1.1-4(c) we have found that these nanostructures lie in a height range of approximately 6-39 nm. We see that both the H and L are dependent upon volume therefore as the volume increases so does the H and L. The L/W ratio shows that the initial shapes of the nanostructures are square however with growth they become rectangular. The L/H ratio is independent of volume as the ratio starts around 3.5-4 then drops to ~2 then with increasing volume it returns to ~3/3.5. This indicated that an equilibrium shape has not been reached. Examining the XRD spectrum in figure 4.1.1-4(d) we see a strong NiO(200) peak at  $2\theta=43.416$  showing that despite not reaching an equilibrium shape this sample also epitaxial. No contamination (Bi) is found.

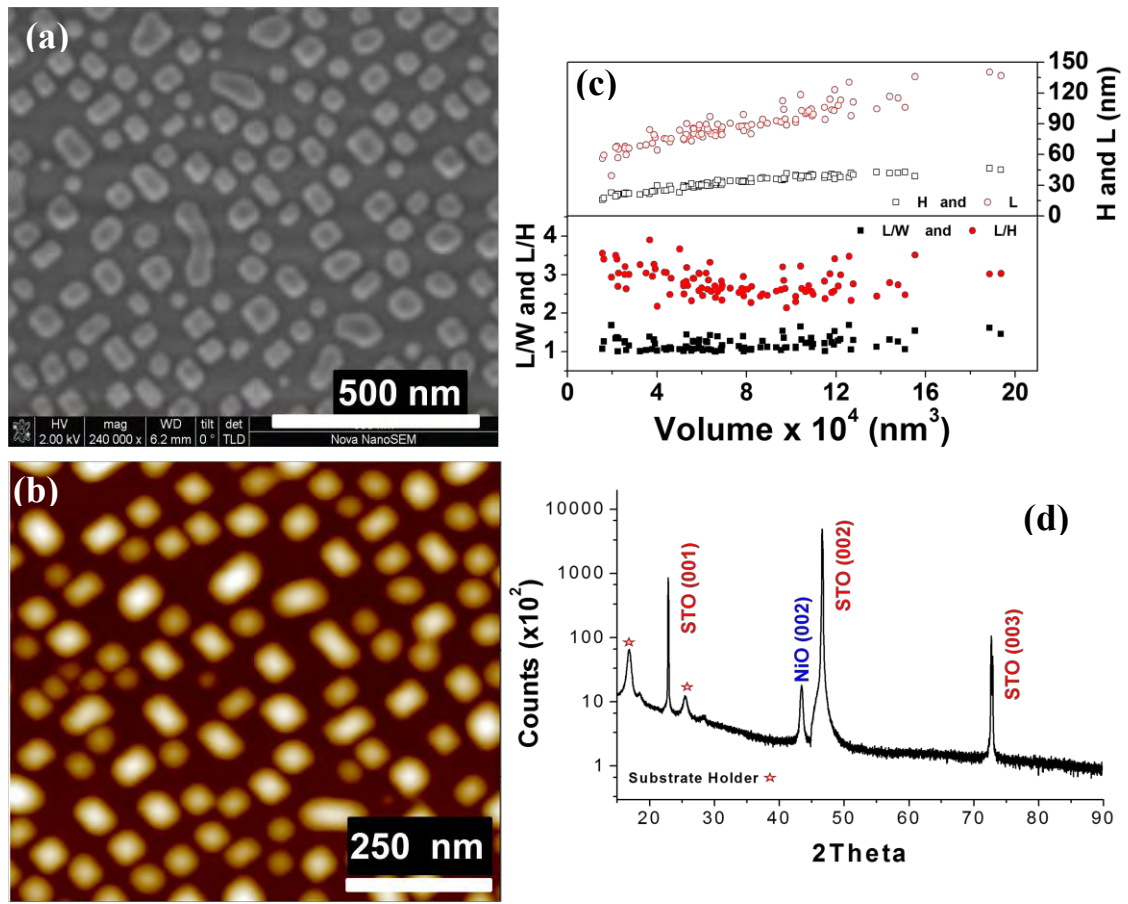


**Figure 4.1.1 -4.** Sample images for depositing in 100 mTorr  $O_2$ , 5 000 pulses, 860 °C and annealing in 1 Torr  $O_2$  on STO (001) (a) SEM (b) AFM (c) Size analysis: Length(L)/Width(W) ratio (black filled square), L/Height(H) ratio (Red filled square), H (black open square) and L (red open square) as a function of nanostructure volume (d) XRD pattern.

Analysing each of these samples we see that using a low deposition pressure of 10 mTorr is not effective in producing any of the desired nanostructures. Here joint maze-like structures are formed. The sample deposited at 35 mTorr shows approximately 95% of the nanostructures being square/rectangular shaped however the XRD shows contamination of Bi. From the comparisons of each pressure it is noted that the most

effective pressure used was 50 mTorr as approximately 95% the nanostructures formed were independent square/rectangular shaped (as with the 35 mTorr sample). This sample however has the required phases present. By increasing the pressure to 100 mTorr, the XRD shows the required data but the morphology of structures present is varied. We see the square structures and slightly rounded structures as well as structures that have not completely formed (or become joined). For all conditions there is a monotonic increase of height and length with respect to volume confirming that these structures are not governed by a strain driven mechanism. We assume that the Ehrlich-Schwoebel (ES) barrier energy for atoms is reached at the base of the facets leading to the transportation of these atom to the top of the nanostructures. This is observed in the homoepitaxy of FCC metals [11; 55; 96]. Figure 4.1.1-5 displays a comparison of the samples with independent nanostructures. This includes the samples of 35, 50 and 100 mTorr.

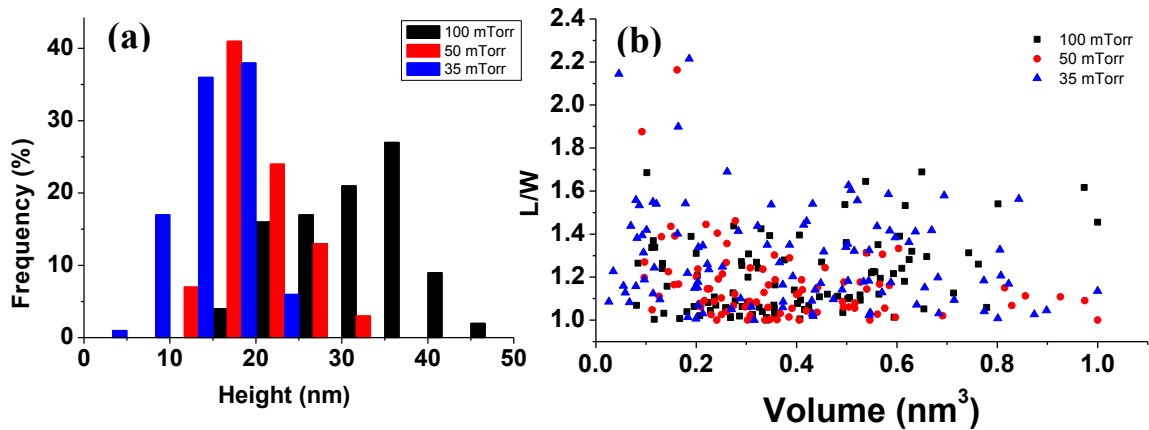


**Figure 4.1.1 -5.** Comparing the pressure variations (a) Height frequency distribution: blue-35 mTorr, red-50 mTorr, black-100 mTorr (b) L/W as a function of volume where: blue triangle-35 mTorr, red circle-50 mTorr, black square-100 mTorr.

Referring to the nanostructure height distribution graph in Figure 4.1.1-5(a) it is possible to compare and contrast the nanocrystal height of the 35, 50 and 100 mTorr samples. From this we see that the average heights extend from approximately 15 to 20 to 35 for the 35 mTorr, 50 mTorr and 100 mTorr samples respectively. The 35 mTorr sample shows the smallest height range and the 100 mTorr shows the largest height range. Then comparing the L/W ratio (surface area) these samples (figure 4.1.1-5(b)) we can see that at lower volumes the 35 mTorr sample has the greatest digression from 1 meaning that the dimensions are the furthest from being square. This sample also has the smallest volume range. The 50 mTorr sample shows a deviation from 1 at lower volumes but as the volume increases the ratio decreases indicating the final shapes to be square. Thus an equilibrium surface area is reached with this sample. Looking at the 100 mTorr sample, the points tend to digress from 1 even as the volume increases illustrating that majority of the shapes are rectangular. For this reason the 50 mTorr sample is given the preference.

The role of pressure is essential in influencing the size as well as inter-particle spacing as demonstrated by the evaluations above. We see pressures lower and higher than that of 50 mTorr (10, 35, 100 mTorr) are insufficient in producing the desired structures and phases as a result of insufficient (lower pressures) and increased (higher pressures) adatomic diffusion. The results of the 50 mTorr sample will therefore be taken into consideration in the next section, being the most effective sample.

## 4.1.2. Varying the Deposition Temperature

In this part of the experiment the deposition temperature was increased from 860 °C to 900 °C to compare and contrast the change. Temperature is known to have an influence of the nanostructure morphology as well as the distance between each nanostructure. A sample was deposited at 900 °C to compare the difference between temperatures of 860 °C and 900 °C. All other parameters were kept constant at a pressure of 50 mTorr, 5 000 pulses, 3 °/minute cooling rate and an annealing pressure of 1 Torr. Figure 4.1.2-1 is the 900 °C sample, which will be discussed in this section. The 860 °C sample (figure 4.1.1-3) has already been discussed in the previous section.

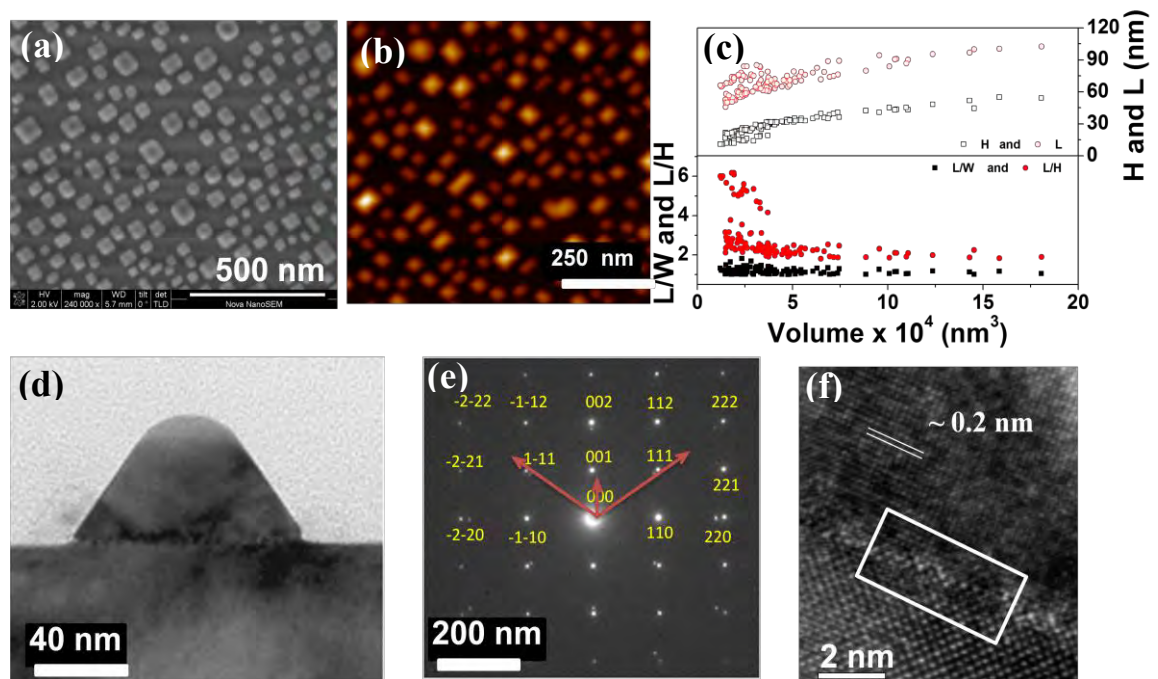


**Figure 4.1.2-1** Sample images for depositing in 50 mTorr O<sub>2</sub>, 5 000 pulses, 900 °C and annealing in 1 Torr O<sub>2</sub> on STO (001) (a) SEM (b)AFM (c) Size analysis

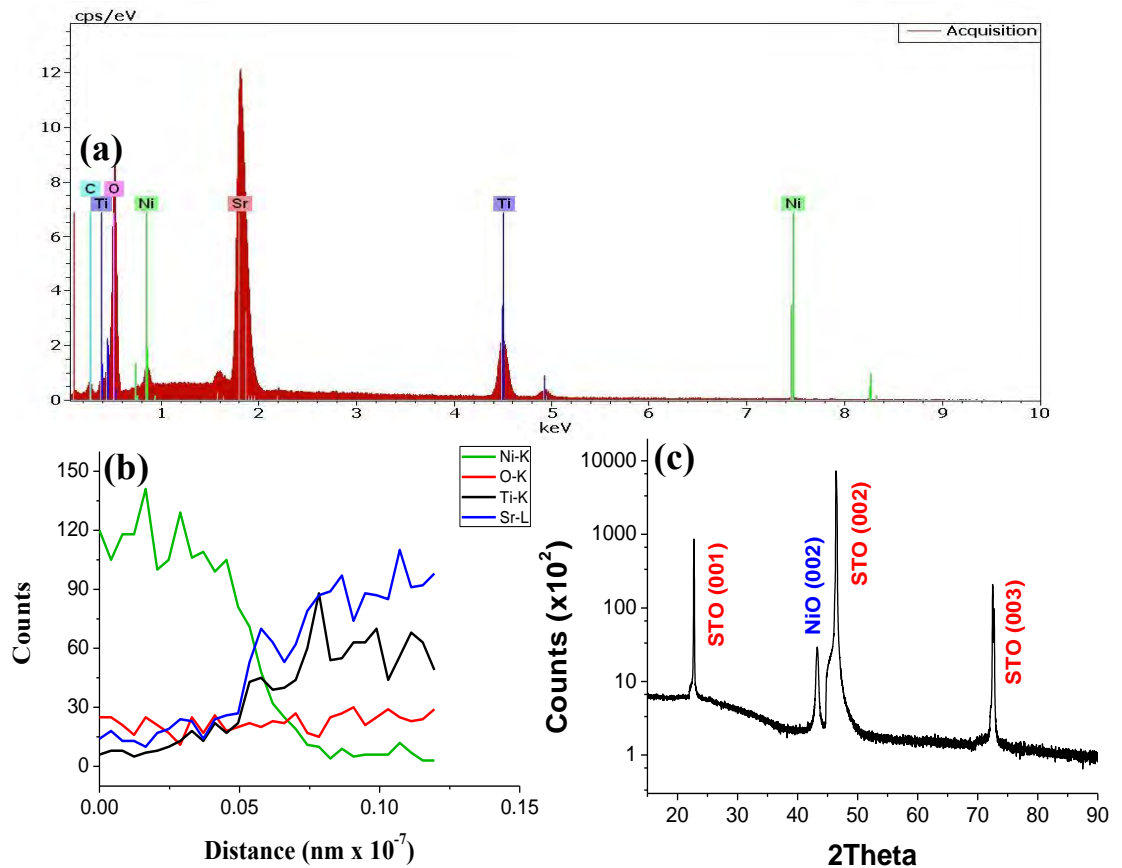
Length(L)/Width(W) ratio (black filled square), L/Height(H) ratio (Red filled square), H (black open square) and L (red open square) as a function of nanostructure volume (d) TEM diffraction pattern (e) HR-TEM (f) XRD pattern.

Figure 4.1.2-1 is a panel of the morphological and structural results obtained on the NiO nanostructure sample deposited at 900 °C. The scanning electron microscopy (SEM) image (Figure 4.1.2-1(a)) along with the AFM image (Figure 4.1.2-1(b)) shows a topographical view of the well dispersed NiO nanostructures on the substrate surface whereby 99 % have the shape of square-pyramids. The dimensions of NiO nanostructures (the average height (H), width (W) and length (L)) were measured using AFM and are plotted as a function of volume in Figure 4.1.2-1(c). A monotonic increase of H and L is observed with no saturation. We note that beyond a critical volume ( $\sim 4 \times 10^4 \text{ nm}^3$ ) the L/W and L/H ratios remain constant at  $\sim 1$  and  $\sim 2$  respectively. For islands smaller than this critical volume, L/W ratios deviate from 1 revealing that the initial shape of islands is rectangular. The concurrence of a constant L/W ratio (surface area) of  $\sim 1$  and a constant L/H ratio that is independent of the volume, for the larger islands indicate that the square shaped islands are at equilibrium. This is not surprising given that NiO has a rocksalt structure with (100) terminations (see TEM data Figure 4.1.2-1(d),(e)). The monotonic increase in individual island dimensions with increasing volume suggest that the shape transition from rectangular to square islands is a volume coarsening transition [55] where the equilibrium shape is influenced by the surface energies of the Nb:STO substrate, the NiO nanostructure facets and the STO–NiO interfacial energy [76; 90].

Figure 4.1.2-1(d) depicts a transmission electron microscope (TEM) image of a NiO nanostructure with an electron diffraction (ED) pattern (Figure 4.1.2-1(e)) acquired along the  $\langle 110 \rangle$  zone axis. Indexing the ED shows each of the nanocrystals to have (001) terminating facets, bound on either side by (111) planes. (111) planes have the highest planar density and minimum interfacial energy in a face centred cubic structure [44; 79]. The presence of distinct spots in the ED confirms the single crystalline nature

of the nanostructure. Figure 4.1.2-1(f) is a high resolution (HR-) TEM image illustrating the growth of single crystalline NiO nanostructure. This image clearly shows the regular arrangement of lattice fringes with inter planar spacing of  $\sim 0.2$  nm, corresponding to the (200) plane of cubic NiO. A rough interface between the island and bottom substrate is observed, attributed to the very large lattice mismatch ( $\sim 7\%$ ) between the NiO and the STO. Figure 4.1.2-2(c) is the x-ray diffraction (XRD) pattern of NiO. The presence of only (001) peaks reveals its epitaxial nature. (JCPDS 01-071-1179). Absence of any XRD peaks related with bismuth or bismuth oxide phases also confirm complete evaporation of Bi from STO surface. The out-of-plane lattice parameter measured from the  $\theta$ - $2\theta$  (200) peak position is  $4.178 \text{ \AA}$ , which matches well with the bulk ( $4.178 \text{ \AA}$ ). This agrees with the TEM data (figure 4.1.2-2(f)) which shows a non-coherent interface between the islands and the substrate, and hence relaxed nanostructures.

Chemical composition spot analysis carried out via energy dispersive spectroscopy (EDS using the SEM) as well as line spectra confirms the presence of Ni, Sr, Ti and O with no residual traces of Bi (Figure 4.1.2-2(a) and (b)). The line scans reveal the percentage of Ni, Sr, Ti and O over a distance through a single nanostructure.



**Figure 4.1.2 -2.** Sample images for depositing in 50 mTorr  $O_2$ , 5 000 pulses, 900 °C and annealing in 1 Torr  $O_2$  on STO (001) (a) EDS using SEM (b) EDS line scans using TEM (c) XRD pattern.

A XRD analysis was carried out on this sample to find the misfit strain between the NiO and STO substrate. Using the values for  $\theta$ , d spacing and the lattice parameters of the bulk STO and bulk NiO (200) (JCPDS values) as well as the calculated STO and NiO (200) (taken from the XRD scan in Figure 4.1.2-2(c)) we are able to find the strain value. The d spacing was calculated using Bragg's law, equation 2.5.1-1 and hence the lattice parameter, a, using the lattice parameter formula for a cubic structure. The misfit in plane and out of plane strain ( $\epsilon_{xx}$ ,  $\epsilon_{zz}$ ) was calculated for NiO(200) and for the NiO(200): STO(200) interaction. For the NiO (200) the out of plane  $\epsilon_{zz}$  value was

calculated using the out of plane lattice parameter calculated (from the spectral scan) and the JCPDS value. This value was found to be a compressive strain of 0.00004787. Then the in plane strain was found to be a tensile strain of 0.00005585. Thereafter the in plane lattice parameter was found to be 4.1782.

The theoretical misfit strain between the film and the substrate: NiO and STO was then calculated to be a tensile strain of 0.06991 in the in plane direction,  $\epsilon_{xx}$ , and a compressive strain in the out of plane direction,  $\epsilon_{zz}$ , at 0.0599. The out of plane lattice parameter was then found to be 4.1923. The calculations for this are as follows:

$$\epsilon_{xx} = \frac{a_{NiO JCPDS} - a_{STO JCPDS}}{a_{STO JCPDS}} \quad 1$$

*Equation 4.1.2-1. Formula for in plane lattice strain for the NiO - STO lattice.*

$$\epsilon_{xx} = \frac{4.1780 - 3.905}{3.905} = \mathbf{0.06991}$$

$$\epsilon_{zz} = \epsilon_{xx} \left( \frac{-2\nu}{1-\nu} \right) \quad 2$$

*Equation 4.1.2-2. Formula for lattice strain using the Poisson ratio. Where  $\nu = 0.3$  for metal oxides.*

$$\epsilon_{zz} = 0.06991(-0.85714) = \mathbf{-0.0599}$$

$$-\epsilon_{zz} = \frac{a_{NiO \text{ calculated}} - a_{NiO \text{ JCPDS}}}{a_{NiO \text{ JCPDS}}}$$

**Equation 4.1.2-3.** Formula for out of plane lattice strain for the out of plane NiO lattice parameter.

$$0.0599 = \frac{a_{NiO \text{ calculated}} - 4.1780}{4.1780}$$

$$a_{NiO \text{ calculated}} = \mathbf{4.428}$$

Since the  $a_{NiO}$  measured value of 4.1778 is lower than the calculated value of 4.428 it indicates that there is an occurrence of strain relaxation. Table 4.1.2-1 summarises these calculated strain values.

**Table 4.1.2 -1.** Parameters calculated for misfit strain and lattice parameters.

Parameters	NiO : NiO <sub>JCPDS</sub>	NiO <sub>JCPDS</sub> : STO <sub>JCPDS</sub>
$a_{zz}$	4.1778	4.428
$a_{xx}$	4.1782	3.9050
$\epsilon_{zz}$	-0.00004787	-0.0599
$\epsilon_{xx}$	0.00005585	0.06991

A more detailed analysis of this sample was conducted as the predominant structures are shown to be more distinctive when compared to the sample at 860 °C (Figure 4.1.1-3). About 99% of the structures formed are square/rectangular pyramidal and the inter-particle distance of the nanostructures are greater in the 900 °C sample thus showing that the nanostructures have completely formed. The XRD in each sample both shows

the expected phases for NiO to prove its epitaxial nature. A comparison of the heights and L/W and L/H of each temperature variation (860 °C and 900 °C) is given in Figure 4.1.2-3 and 4.1.2-4.

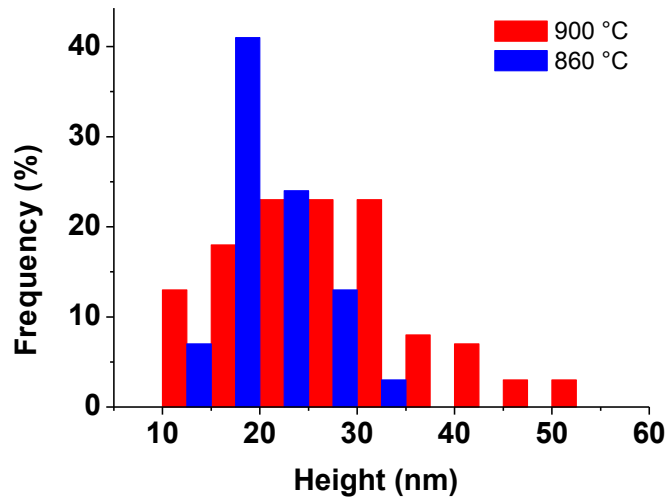


Figure 4.1.2 -3. Comparing the temperature variations: height frequency distribution.

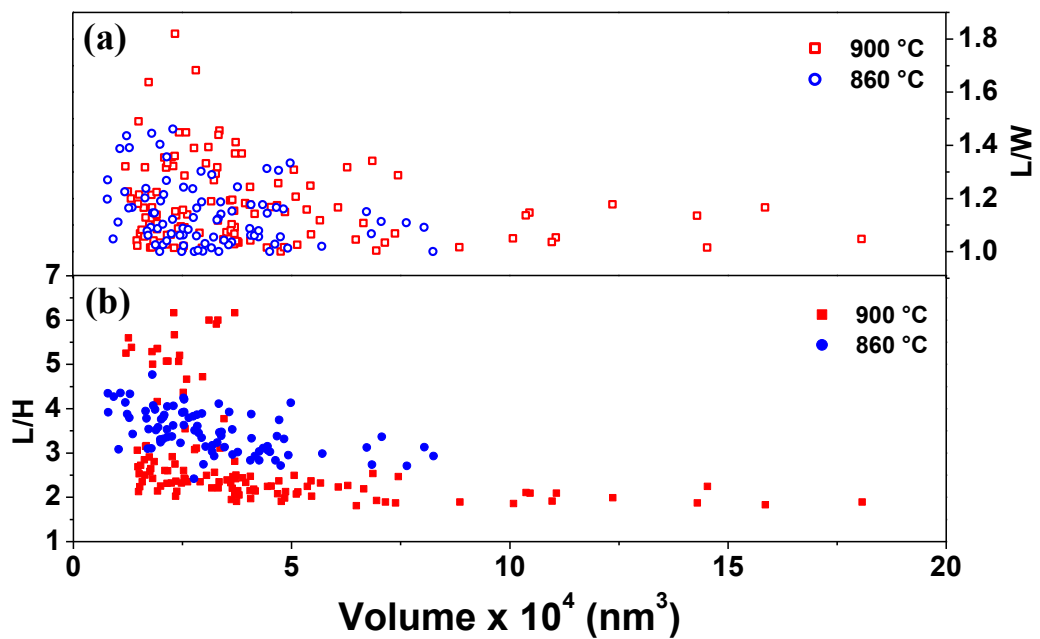


Figure 4.1.2 -4. Comparing the temperature variations as a function of volume (a) L/W (b) L/H.

The distribution of nanocrystal height in figure 4.1.2 -3 shows a limited height range for the 860 °C sample when compared to the 900 °C sample which starts around 10 nm and ends around 52 nm. In the 860 °C sample the average height range lies around the 18 nm mark whereas the 900 °C has an average height around the 25 nm mark. Another structural comparison, the L/W or surface area (Figure 4.1.2 -4) shows the 900°C sample to have a greater volume. At low volumes both samples show the initial structural shape to be rectangular however the 900 °C sample has more deviation from 1. As the volume is increased both samples drop to a ratio of ~1 showing the final shape is square. When comparing the L/H, the 860 °C sample shows points scattered around the ratio of 3 whereas the 900 °C sample shows a constant ratio of 2 after a critical volume ( $\sim 4 \times 10^4 \text{ nm}^3$ ). This suggests that the square structures of the 900 °C sample has reached equilibrium and those of the 860 °C sample have not. The next section investigates the effect of varying the laser pulses.

### **4.1.3. Varying the Number of Laser Pulses**

A variation in the number of laser pulses was then undertaken to determine the effect on the shape of nanocrystals. The number of laser pulses used during deposition influences the substrate surface and hence nanocrystal volume as it controls how much material is ablated and deposited onto the STO substrate surface. The volume along with temperature controls the shape of the nanostructure as well as the facet orientations to result in pyramidal hut shaped structures [76]. By increasing the number of pulses it will be possible to discover the maximum growth (height) of the nanostructures before it starts expanding outwards, becoming a merged structure or even a film. Here we see the

formation to truncated pyramids and finally joined hexagons (a flat surface). The volume along with the misfit strain has a significant impact on this transition and hence on the morphology and shape evolution of the nanostructures [55]. Figure 4.1.2 -1/ 4.1.2 -2 is seen to be the optimum sample therefore the following depositions will keep the same deposition/annealing parameters but vary the pulses. By comparing figure 4.1.2 -1/4.1.2 -2 to 4.1.3-1 and 4.1.3-2, whereby the pulses increase from 5 000 to 10 000 and 20 000 respectively, it can be seen that the square/rectangle nanocrystal formation is diminished with the increase of laser pulses.

The number of pulses in Figure 4.1.3-1 were increased to 10 000. Looking at the SEM image in Figure 4.1.3-1(a) and comparing this sample to the sample deposited at 5 000 pulses (see figure 4.1.2 -1/4.1.2 -2) we see the formation of ~90% rounded, joint structures resembling truncated pyramids. There are also ~10% of the square/rectangular pyramidal shaped structures as well. A height determination can be made though the acquired AFM image in Figure 4.1.3-1(b). The heights of these structures are shown to be about 55 nm. Therefore we can state this is the maximum height before the structures expand in a lateral direction.

Confirmation that this sample is also epitaxial is given by the XRD spectrum in Figure 4.1.3-1(c) which shows a strong NiO(200) peak at  $2\theta=43.288$ . The lattice parameter is calculated to be 4.175 which is significantly lower than the optimum sample and the bulk (4.178). The XRD scan shows that all the bismuth has evaporated from the sample.

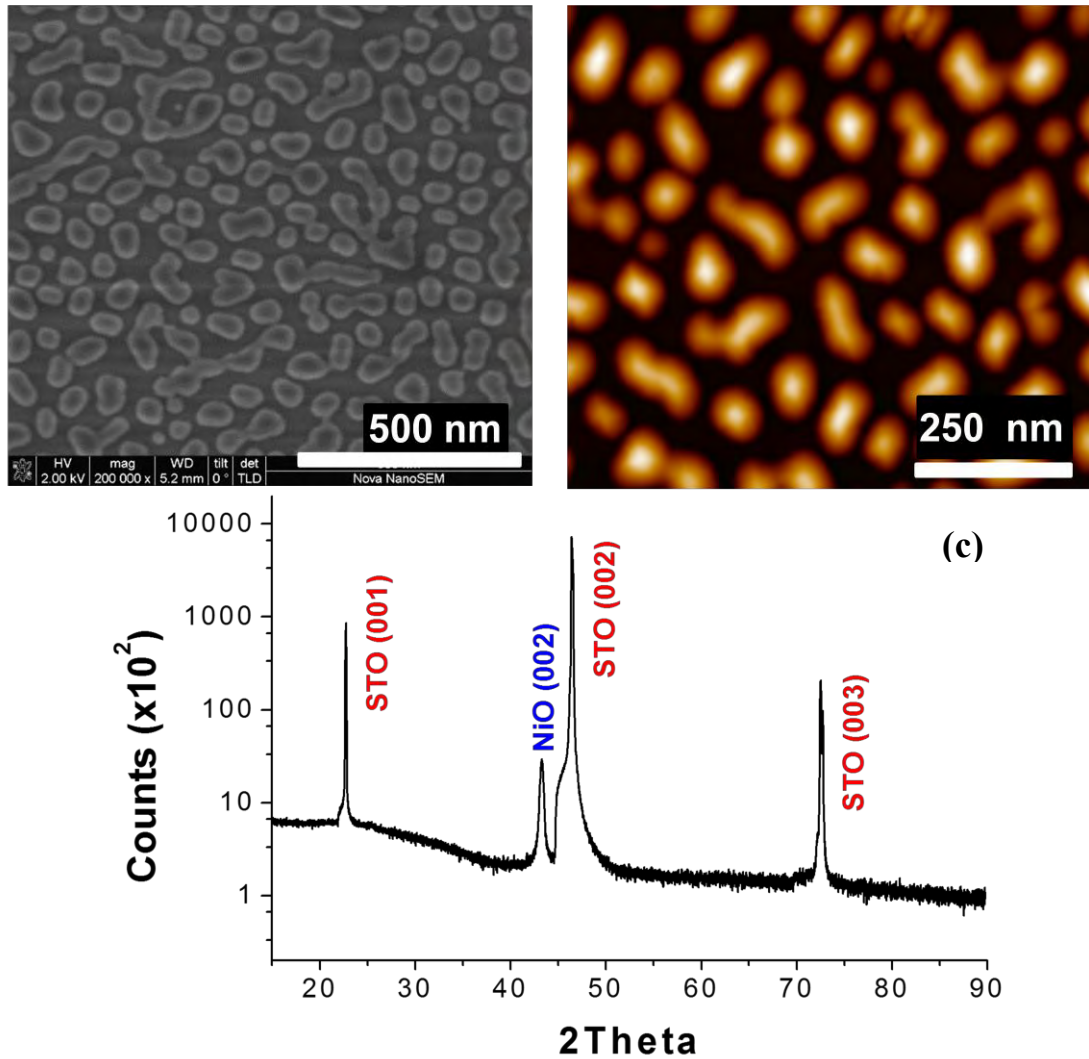


*Figure 4.1.3-1. Sample images for depositing in 50 mTorr O<sub>2</sub>, 10 000 pulses, 900 °C and annealing in 1 Torr O<sub>2</sub> on STO (001) (a) SEM (b) AFM (c) XRD.*

Next the number of pulses was increased to 20 000 and unlike its predecessors this sample shows no nanostructure formation but a film-like growth as seen in the SEM (Figure 4.1.3-2(a)). Comparing the AFM in figure 4.1.3-1(b) image to that in Figure 4.1.3-2(b), we see that the nanostructures have expanded laterally and hence have joined to form a film with a few gaps in between. This shows that the conditions used have resulted in a height constraint and therefore the production of a metastable state of ‘joined hexagonal’ structures. This means that the minimum energy barrier has not been

achieved for the formation of pyramidal structures [76]. Analysing the height of these formations shows them range from 15–45 nm.

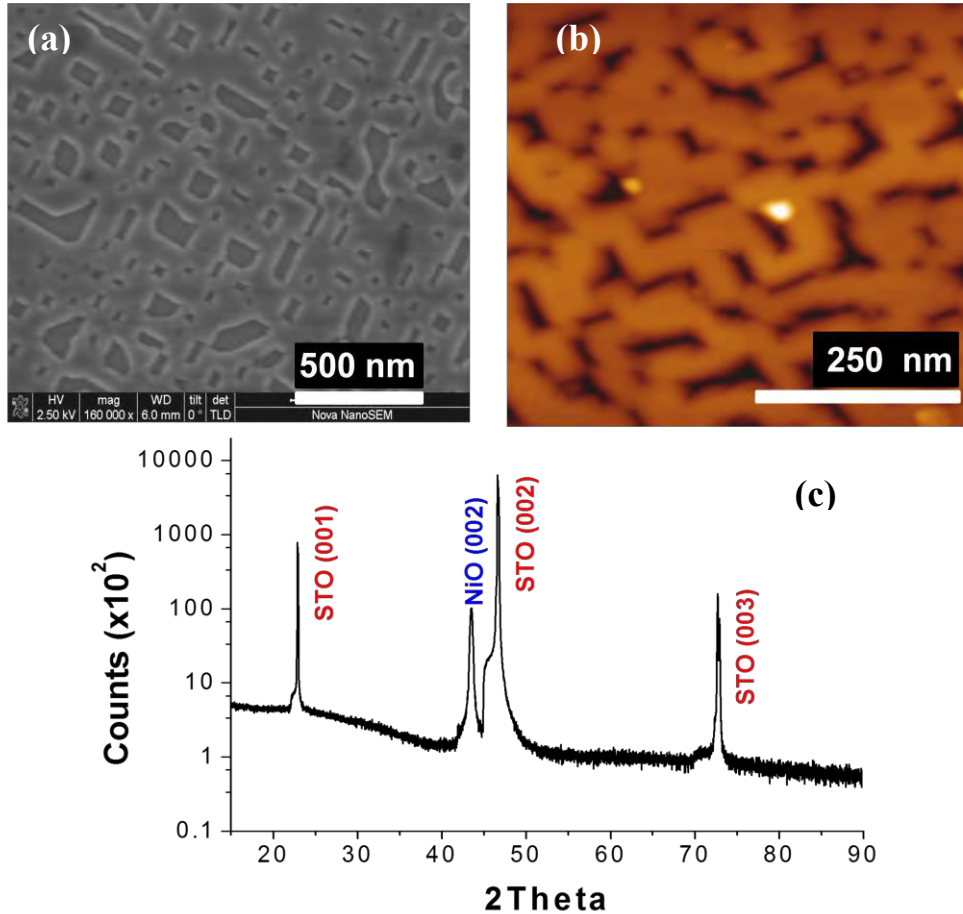


**Figure 4.1.3-2.** Sample images for depositing in 50 mTorr O<sub>2</sub>, 20 000 pulses, 900 °C and annealing in 1 Torr O<sub>2</sub> on STO(001) (a) SEM (b) AFM (c) XRD.

The XRD spectrum of this sample (Figure 4.1.3-2(c)) also shows a strong NiO(200) peak which is at  $2\theta=43.485$  and a lattice parameter of 4.157 which is much lower than the previous samples. This indicates that there is a greater lattice mismatch between the NiO and STO substrate as the pulses are increased and therefore results in the morphology seen in the SEM images. This sample is also epitaxial as seen from the

(001) order of reflection is present. No bismuth contamination is found in this sample as well.

From these analyses, we can state that the maximum height for the pyramidal formation is ~55 nm after which the formation of a film-like structure spanning out to ~45 nm is prevalent.

#### **4.1.4. Varying the chamber pressure during Annealing**

The annealing pressure also has a significant effect of the outcome of the film morphology as well as the phase formation. Annealing in a vacuum and annealing in different oxygen pressures are compared whereby the before-annealing results can be viewed and subsequently the post-annealing results. Samples were deposited followed by annealing in a vacuum environment and in an oxygen partial pressure environment including 100 mTorr and 1 Torr. The 1 Torr oxygen environments is show to be the most successful in producing the desired morphology of nanostructures as well as the appropriate NiO phase. Annealing in a vacuum leads to Ni<sub>2</sub>O<sub>3</sub>.

Initially a sample was deposited onto STO (001) at a temperature of 860 °C, in an O<sub>2</sub> pressure of 35 mTorr, with 10 000 pulses, cooled at 5 °/min and then annealed for 2 hours at 900 °C in a vacuum environment. Despite film-like structure shown in the SEM (Figure 4.1.4 -1(a)) the sample was epitaxial as confirmed by the XRD in Figure 4.1.4 -1(b). The post annealing results show the formation of rounded structures as seen in the SEM (Figure 4.1.4 -1(c)). Upon analysis via XRD, we observe that these structures are in fact Ni<sub>2</sub>O<sub>3</sub>(112) instead of the required NiO(200) phase (Figure 4.1.4 -1(d)).

Therefore annealing in a vacuum leads to an increase in oxidation state and hence the production of  $\text{Ni}_2\text{O}_3$ .

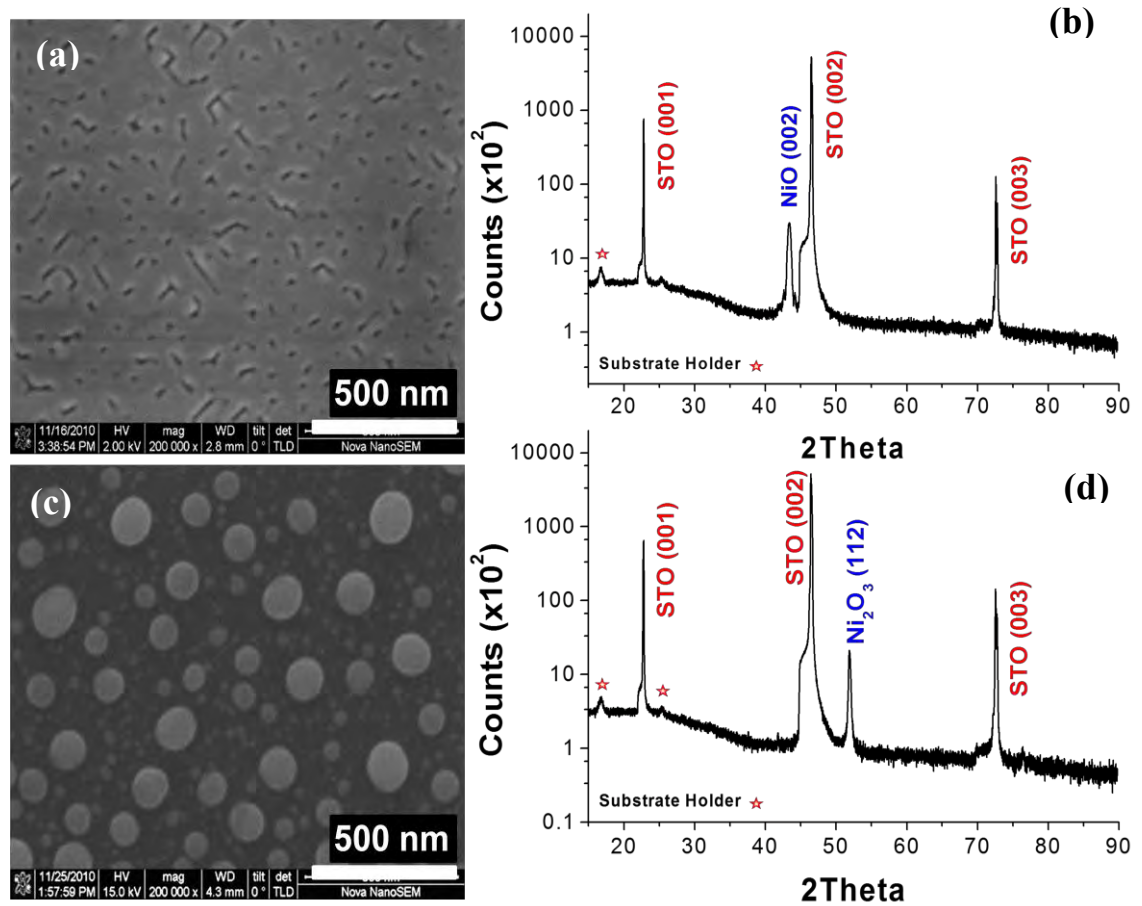


**Figure 4.1.4 -1.** Sample images for depositing in 35 mTorr  $\text{O}_2$ , 10 000 pulses, 860 °C and annealing in a vacuum on STO (001) (a) SEM before annealing (b) XRD pattern before annealing (c) SEM after annealing (d) XRD pattern after annealing.

To examine the converse of annealing in a vacuum we annealed for 2 hours in a partial oxygen environment. First the effects on the morphology at 100 mTorr were examined and proved to be insufficient, thereafter annealing at 1 Torr was carried out.

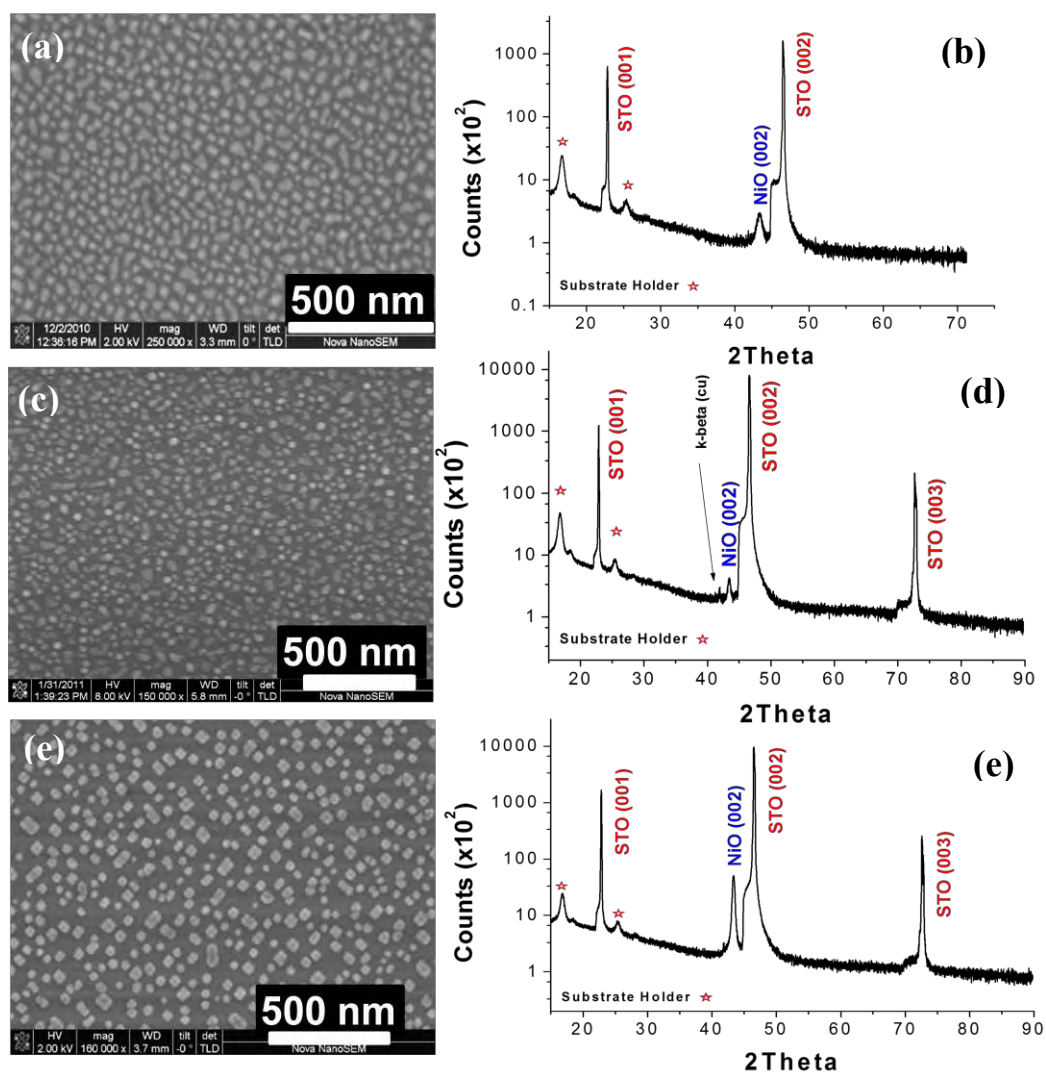


**Figure 4.1.4 -2.** Sample images for depositing in 50 mTorr  $O_2$ , 5 000 pulses, 860 °C and annealing in 100 mTorr  $O_2$  and 1 Torr  $O_2$  on STO (001) (a) SEM before annealing (b) XRD before annealing (c) SEM after annealing in 100 mTorr  $O_2$  (d) XRD after annealing in 100 mTorr  $O_2$  (e) SEM after annealing in 1 Torr  $O_2$  (f) XRD after annealing in 1 Torr  $O_2$ .

Figure 4.1.4-2 displays a sample deposited onto STO (001) at a temperature of 860 °C, in an  $O_2$  pressure of 50 mTorr, with 5 000 pulses, cooled at 3 °/min in a vacuum and

then annealed for 2 hours at 900 °C in 100 mTorr O<sub>2</sub> then a second annealing attempt was carried out at 1 Torr O<sub>2</sub> for 2 hours at 900 °C.

The before annealing SEM image in Figure 4.1.4-2(a) shows the formation of individual nanostructures of varied shapes and sizes; some have a square/rectangle appearance and others show joined structures. Looking at the XRD spectrum we see the required NiO (200) showing the epitaxial nature of the sample. After the first annealing attempt we see the almost defined nanostructures in the before annealing sample has become rounded with no distinct edges. These structures resemble random formations as seen in the SEM images in Figure 4.1.4-2(c). The XRD plot in Figure 4.1.4-2(d) does however show it to be epitaxial with the expected NiO(200) phase. After conducting a second annealing attempt we see well-defined discrete nanostructures in the SEM image in Figure 4.1.4-2(e). Examining the XRD we find epitaxial growth having only the NiO(200) phase and (001) order of reflections for the STO.

In summary, we see that annealing in vacuum results in unwanted Ni<sub>2</sub>O<sub>3</sub> phases and annealing in a 100 mTorr partial O<sub>2</sub> environment is not sufficient in producing discrete faceted nanostructures. We therefore postulate that annealing in 1 Torr of O<sub>2</sub> partial pressure is required to promote crystallisation and equilibrium shape formation in nanostructure as well the required phase formation. For this reason an annealing step at 1 Torr has been accepted in the production of equilibrium square pyramidal nanostructures.

## **CHAPTER 5. RESULTS AND DISCUSSION**

### **(RESISTIVE SWITCHING EFFECT)**

#### **5.1. I-V measurements**

Resistive switching behaviours of individual NiO nanostructures were investigated using the C-AFM mode of a JEOL SPM 5400 under sample biased conditions. A voltage sweep from -8 V to 0 V to +8 V (positive) and +8 V to 0 V to -8 V (negative) was applied. A clean tip-surface contact was ensured by checking the I-V characteristics of bare portion of the conductive substrate (see Figure 5.1-2). The switching performance of these nanostructures as a function of height and size within this sweeping voltage range was then investigated.

Reports on resistive switching primarily reveal two switching types based on the manner in which the applied bias changes the resistance state. One is unipolar switching in which two stable resistance states can be achieved by switching voltages with the same polarity. Bipolar switching on the other hand requires switching the voltage with opposite polarities to induce bistable resistance states. The I-V curves acquired on NiO nanostructures of varying height (15 nm (black), 23 nm (red), 30 nm (blue)) as displayed in Figure 5.1-1(a) reveal a bipolar resistive switching type.

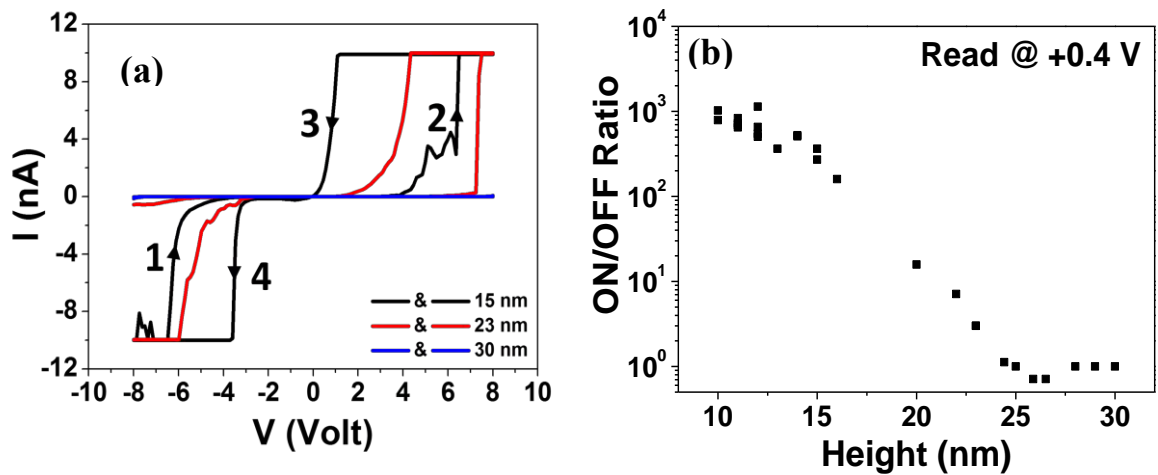


**Figure 5.1 -1.** Resistive switching characteristics of the NiO nanostructures. (a) *I-V* measurements taken at heights 15 nm, 23 nm, 30 nm in black, red, blue respectively. (b) ON/OFF ratio versus height.

In the case of 15 nm high nanostructures, during the positive sweep (from -8 V to 8 V) (region 1 in Figure 5.1-1(a)) at -8 V high current ( $\sim 10$  nA) flows through the device. As the applied voltage (field strength) is swept from -8 V to 0 V a sudden drop off in the current is observed at -4 V and afterwards a minimum current state is observed up to 0 V. With further raise in the applied voltage from 0 to +8 V (region 2) exponential increase in the current is observed after +3 V and reaches high current limit (10 nA) at +6.5 V. Saturation current, observed in the graph after +6.5 V, is due to the imposed current compliance by the AFM hardware. However, during negative sweep (from 8 V to -8 V) high current flows through the junction even when the voltage is swept to lower positive side. When the applied voltage decreases below +1 V, decreasing field strength causes an exponential decrease in the current, as seen in region 3. With subsequent sweeping in the negative region (from 0 V to -8 V) low current state flows till -3 V, whereas, an abrupt increase in the current is observed with continued negative sweep till

-8 V (region 4). Distinct I-V characteristics observed during positive and negative voltage sweep develop a loop, which have low current state (or high resistance state-HRS) and high current state (or low resistance state-LRS) in both regions, respectively. This kind of resistive switching under applied bias is reproducible on each of the NiO nanostructures over a few tens of switching loops, where the ON/OFF ratio (measured at a read voltage of +0.4 V) was found to be approximately  $3 \times 10^2$ . Remarkably the NiO nanostructures show very low reset currents of 10 nA (in LRS), which is crucial for high density integration of ReRAM device. This low reset current is attributed to the small contact radius between the top electrode and the conductive AFM tip ( $\sim 10$  nm), which generates locally concentric fields in the NiO nanostructure. I-V loops were observed for the 23 nm high nanostructure (red) were significantly lower with an ON/OFF ratio  $\sim 3$  (at a read voltage of +0.4 V). However, no switching I-V loops are observed for nanostructures of heights greater than  $\sim 30$  nm which hint that there may be a dependence of the switching behaviour on the height of the nanostructure. Therefore, switching I-V loops were recorded for NiO nanostructures of different heights and plotted in terms of ON/OFF ratio (measured at a read voltage of +0.4 V), as shown in Figure 5.1-1(b). Figure 5.1-1(b) shows the ON/OFF ratio decreases with an increasing nanostructure height up to  $\sim 25$  nm. Beyond this height, no switching action is observed within the working voltage range.

To further understand the role of the nanostructure height, local switching behaviors of a single NiO nanostructure were recorded at various points of the nanostructure using the C-AFM tip. Figure 5.1-2(a) show topographical locations of four different points on/near a pyramidal NiO nanostructure of height  $\sim 26$  nm. Figure 5.1-2(b) is a plot of the acquired switching I-V loops. Similar measurements were performed on different nanostructures.

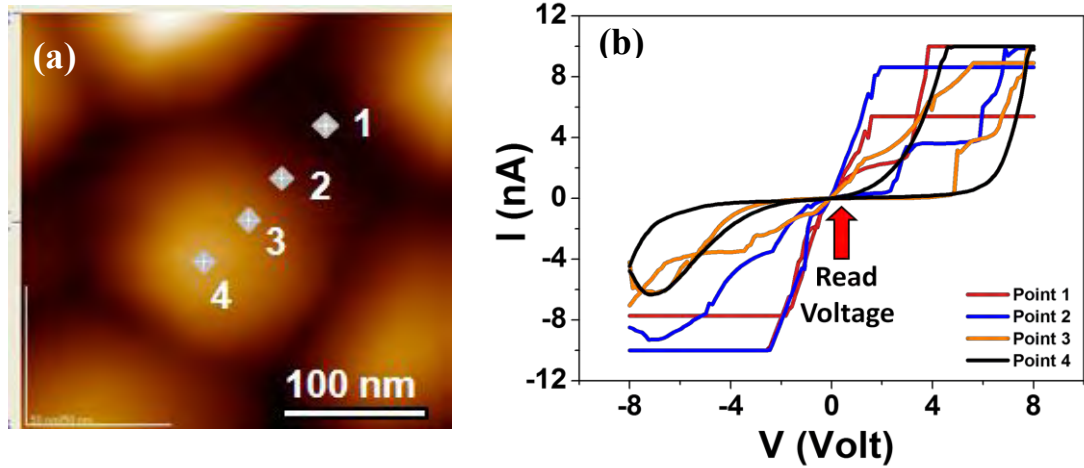


**Figure 5.1 -2.** Resistive switching characteristics of an individual NiO nanostructure.

(a) Points 1 – 4 are various heights along an individual nanostructure. (b) I-V measurements taken at points 1-4. Point 1 (red - 0 nm), point 2 (blue - 10 nm), point 3 (orange - 20 nm) and, point 4 (black - 26 nm).

To ensure that the measurements are not convoluted by the tip-surface interface, we first performed an I-V analysis on a bare portion of the Nb:STO substrate. I-V data recorded at point 1 clearly shows a linear current increase with applied field indicating good conducting characteristics of the bottom electrode (Nb:STO). At point 2, where the C-AFM tip is at the base of the NiO nanostructure (height  $\sim 10$  nm), we see that as the applied bias is increased beyond +2 V an abrupt increase in the current switches the initial HRS state of the local region on the nanostructure to LRS with a ON/OFF ratio  $8 \times 10^2$  (read voltage +0.4 V), however, the subsequent voltage sweeps generate a memristive switching loop (blue lines in Figure 5.1-2(b)). As the tip is moved further on the nanostructure at point 3 and 4 (height  $\sim 20$  and 26 nm), I-V loops were observed with set voltage of +5 and +6.5 V, respectively (orange and black line in Figure 5.1-2 (b)). The ON/OFF ratio here is found to be  $2 \times 10^1$  and 1 respectively at a read voltage of +0.4 V, thus indicating a direct proportionality of the set voltage and ON/OFF ratio

to the height of the nanostructure. In addition to this, switching measurements were performed on nanostructures of fixed height 15 nm, but varying lateral areas from  $\sim 10^4$  to  $10^5$  nm<sup>2</sup>. In this case, the ON/OFF ratio ( $5 \times 10^2$ ) was found to be independent of the lateral area of the nanostructure (figure 5.1-3) which underlies that the observed switching effect is an interface effect rather than an electroforming/filamentary mechanism [45].

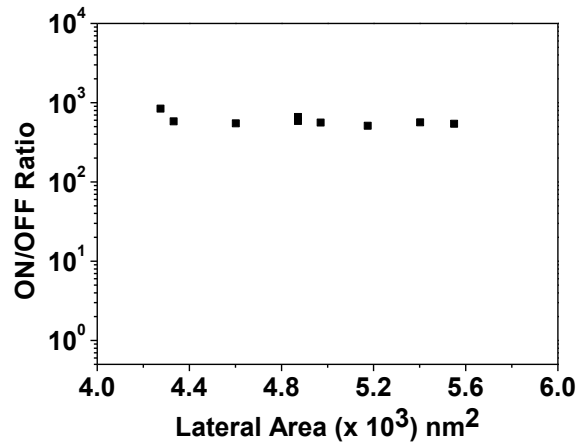


*Figure 5.1 -3. ON/OFF ratio vs. Lateral area plot.*

## 5.2. Resistive Switching Mechanism

For further analysis of the origin of this switching behaviour, numerical fitting of the obtained I-V loops was conducted, shown in Figure 5.2-1. For linear fitting of I-V curves we have considered three leakage mechanisms as follows [66];

$$I \propto \frac{8}{9} \epsilon_r \epsilon_0 \mu \frac{V^2}{d} \quad \mathbf{1}$$

*Equation 5.2 -1. Formula for Space charge limited (SCL) conduction.*

$$\ln I \propto \sqrt{\frac{e^3}{4\pi\epsilon_r\epsilon_0 d}} / kT \cdot \sqrt{V} \quad 2$$

**Equation 5.2 -2.** Formula for Schottky emission (SE).

$$\ln I \propto \sqrt{\frac{e^3}{\pi\epsilon_r\epsilon_0}} / rkT \cdot \sqrt{V} \quad 3$$

**Equation 5.2 -3.** Formula for Poole-Frenkel (PF) emission.

Where,  $I$  is the current,  $V$  is the applied voltage,  $\epsilon_r$  is the relative dielectric constant of material,  $\epsilon_0$  is the permittivity of free space,  $\mu$  is the mobility of charge carriers,  $e$  is the electric charge,  $k$  is the Boltzmann's constant,  $T$  is the temperature,  $E$  is the electric field and  $d$  is the thickness.

The I-V curve plotted on a *log-log* scale (shown in Figure 5.2-1(a)) indicates that LRS follows Ohmic behaviour with slope of 1. However, best fit for the HRS is found only to an  $\ln I$  Vs  $V^{1/2}$  behaviour with a slope of 3.43 (Figure 5.2-1(b)) thus following Schottky emission. The dielectric constant calculated from the HRS slope is  $\sim 4.7$ ; lower than the reported bulk value. This is consistent with previous reports where oxygen diffusion from the bottom electrode (Nb:STO) at high growth temperatures is expected to influence the defect structure of NiO during synthesis, resulting in relatively lower dielectric constant [15].

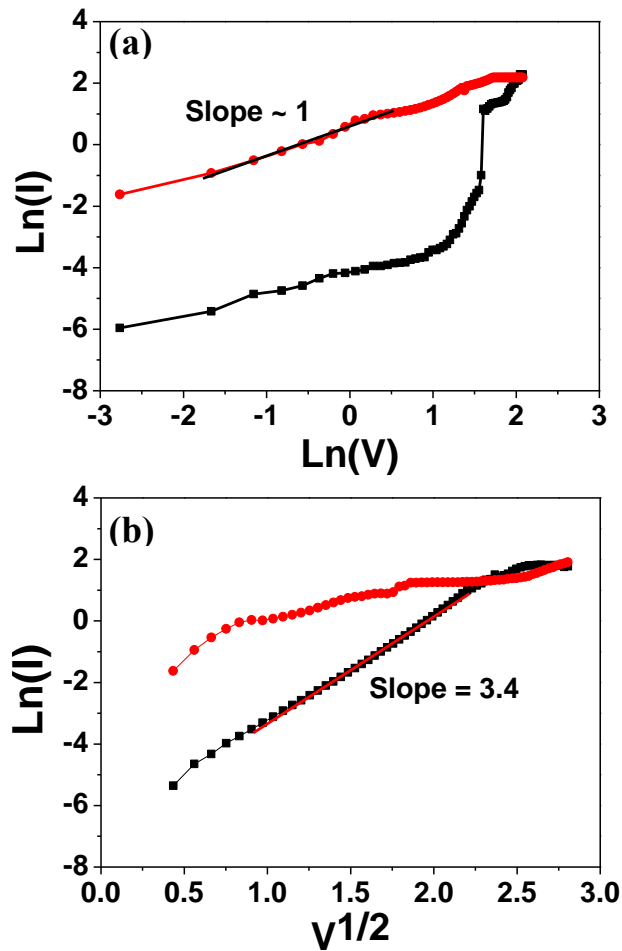


**Figure 5.2 -1.** Linear fitting results of (a) LRS in bipolar switching with Ohmic conduction and (b) for HRS which show Schottky emission conduction behavior in a 15 nm high nanostructure.

### 5.3. A detailed analysis of the conduction mechanism in NiO/Nb:STO

It is well known that Nb:STO shows n-type semiconducting properties and oxygen vacancies (act as minority carriers) are generated at the high growth temperatures. In contrast, NiO is p-type semiconductor where the minority carriers are electrons or excess oxygen ions [40]. Thus the NiO/Nb:STO structure forms a well defined p-n junction with a potential barrier as demonstrated in Figure 5.3-1(a) along with a

schematic of band diagram (Figure 5.3-1(b)). Figure 5.3-1(b) also shows the electron affinity and resultant barrier heights for p- and n-type regions [40; 93]. The barrier height for electrons is  $\sim 0.4$  eV higher than holes; therefore we expect electrons to dominate the current. At equilibrium conditions, first a barrier or depletion region is formed at the NiO/Nb:STO interface, as shown in Figure 5.3-1(b). Generally, this depletion width in p-n junction device can be estimated using Schottky model and the equations are expressed as follows:

$$d_p = \left( \frac{2\varepsilon_r\varepsilon_0V_D}{e} \frac{N_D/N_A}{N_A+N_D} \right)^{1/2} \quad \mathbf{1}$$

$$d_n = \left( \frac{2\varepsilon_r\varepsilon_0V_D}{e} \frac{N_A/N_D}{N_A+N_D} \right)^{1/2} \quad \mathbf{2}$$

**Equation 5.3 -1, 5.3 -2.** Depletion width. Where,  $d_p$  and  $d_n$  are depletion width along NiO and Nb:STO side from interface,  $V_D$  is diffusion voltage, and  $N_A$  and  $N_D$  are concentration of majority carriers in NiO and Nb:STO.

Utilizing the estimated value of relative dielectric constant of NiO (4.7) and standard dielectric constant of Nb:STO, in above equation (5.3-1) and (5.3-2) the width of depletion region at the interface is found to be 5.4 nm in NiO and 20.6 nm in Nb:STO.

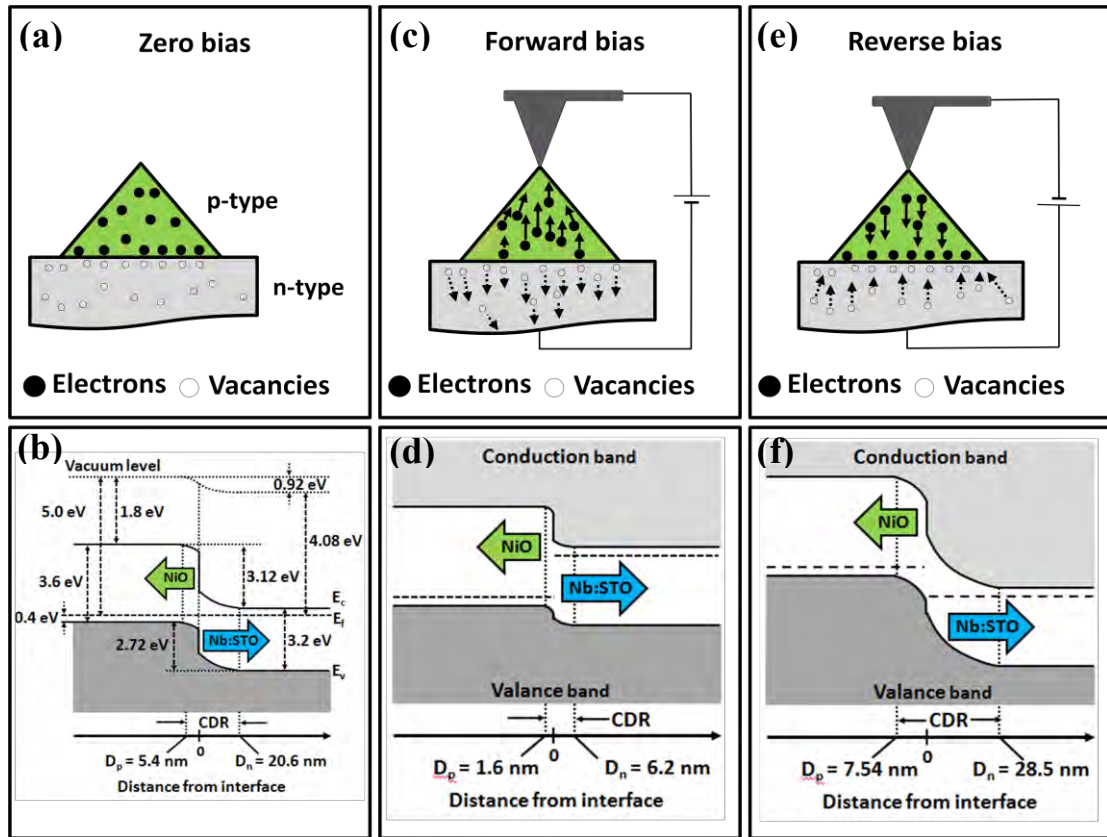


**Figure 5.3 -1.** Schematic of conduction mechanism in NiO/Nb:STO p-n junction and its respective band diagram at zero bias (a) and (b), forward bias (c) and (d), and reverse bias (e) and (f). Width of depletion region has been calculated for 1 V applied in forward and reverse bias.

Under forward bias the junction behaves as a classical p-n junction where at high enough electric field, the negatively charged electrons or oxygen ions in NiO and positively charged oxygen vacancies migrate away from the interface (Figure 5.3-1(c)). This results in decreasing width of depletion region (Figure 5.3-1(d)), giving rise to a sudden increase of current. The estimated depletion width under forward bias (+1 V) is found to be 1.65 nm in NiO and 6.22 nm in Nb:STO region, respectively. When the

applied field decreases below a threshold point, the field strength decreases which results in a corresponding decrease in the current. When reverse bias is applied, the oxygen vacancies in Nb:STO and the excess oxygen ions in NiO drifts towards the junction, Figure 5.3-1(e). Consequently the minority carrier concentration in the vicinity of the junction interface rises causing an increase in the depletion width (which result in low conducting state or HRS), as shown in Figure 5.3-1(f). The estimated depletion width (at -1 V) is found to be 7.54 nm in NiO and 28.5 nm in Nb:STO region, respectively.

It is the large currents under strong reverse bias conditions that are intriguing. Under a sufficiently strong applied reverse bias, the measured current jumps to a magnitude well above the saturation threshold of the C-AFM hardware. Typically for a p-n junction under reverse bias, such large currents are associated with either Zener (tunnelling) breakdown or Avalanche breakdown. Using the well-known expression for electric-field distribution in a dielectric medium under an AFM tip [81], we obtain an electric field strength of  $\sim 10^6$  V/cm for a typical nanostructure. This results in a tunnelling probability of close to zero [61]. Furthermore this field strength is nowhere sufficient to create an avalanche breakdown. Thus we rule out either of these mechanisms. Also the lack of a metal (such as Au, Pt etc) as a bottom electrode [15] as well as no dependency on the lateral area means that filamentary mechanisms are also precluded. On the other hand, oxide interfaces have oxygen vacancies as minority carriers. Indeed, modulation of oxygen vacancies at a heterointerface under electric bias and the resultant point defect transport towards the interface was shown to drive the switching process for similar heterostructures [40; 43; 74]. The calculated field strength is high enough to create an injection of minority carriers at the interface, which give rise to drift current under an electric field, and hence the high conducting state (LRS) of the device. The

overall behaviour according to the applied bias agrees with the switching polarity shown in Figure 5.1-1(a). Therefore, we posit that the electric-field induced change in the minority carrier concentrations at the interface controls the bipolar resistance switching behaviour.

Structurally we note that the interface has the features required to satisfy our model. The presence of a rough interface between the NiO and the Nb:STO cathode offers a number of defect paths for the vacancies migration to occur. It also follows for shorter structures, the electric field is always strong enough to heavily modulate interface, which results in the observed conductivity. Conversely for higher islands, the field is simply not strong enough to create the required changes at the interface.

## CHAPTER 6. CONCLUSIONS

In conclusion, we have successfully fabricated epitaxial NiO nanostructures on (001) STO (and Nb:STO) substrates employing the concept of perovskite instability and phase separation followed by bismuth oxide evaporation. The pressure, temperature, laser pulses and annealing chamber O<sub>2</sub> partial pressure were varied in order to determine the optimum conditions whereby the nanostructures adopt planes with the highest planar density and minimum interfacial energy of a face centred cubic structure [44; 79]. Manipulation of the deposition and annealing parameters show strong influence on the distribution of nanostructures, their shape and composition.

Changing the oxygen partial pressure during the deposition process showed the influence pressure has on the surface area to volume ratio as well as the inter-particle spacing. From this we found the optimum pressure to be 50 mTorr as the square pyramid structures begin to undertake an equilibrium shape. We also found that partial oxygen pressures of 10 mTorr and below do not support the formation of discrete nanostructures, 35 mTorr is not adequate for the removal of bismuth oxide, and 100 mTorr does not assume an equilibrium shape as the structures grow. Analysis of the effects of temperature modification was observed between samples deposited at 50 mTorr with temperatures of 860 °C and 900 °C. Here we found that the 900 °C sample had a wider height and volume range. These structures showed the evolution to an equilibrium shape whereas the 860 °C sample did not. The 900 °C conditions were therefore used as the optimum. The maximum nanocrystal shape was then uncovered by increasing the laser pulses from 5 000 to 10 000 and finally 20 000. Here we saw that the nanostructures grew to ~55 nm high at 10 000 pulses after which a film-like growth started to dominate. This flattened out to approximately ~45 nm high. Examination of

the annealing chamber conditions were undertaken in order to find the optimal conditions for phase formation and crystallisation of the nanocrystals. From this we found 1 Torr to facilitate this. Lower annealing chamber pressures (100 mTorr) resulted in rounded, undefined nanostructures and annealing in a vacuum left behind completely rounded nanostructures of Ni<sub>2</sub>O<sub>3</sub> phases.

Altogether we have found the optimum conditions to be depositing in an oxygen partial pressure of 50 mTorr O<sub>2</sub>, at a temperature of 900 °C with 5 000 laser pulses and thereafter annealing in a chamber partial oxygen pressure of 1 Torr. Topographical and chemical analysis reveals phase pure pyramidal shaped NiO nanostructure.

We investigated the resistive switching properties of these optimised NiO nanocrystals, in which the nanoscale islands were individually addressed. Typical extrinsic bipolar switching properties have been observed and a pronounced effect of nanostructure height on the switching voltage has been found. We observe this effect in a height range of ~10-23 nm. Lower nanostructure heights show conductive behaviour with no switching whereas the taller heights show a strong resistive behaviour. The ON/OFF ratio is shown to decrease with an increasing height up to ~25 nm, as beyond this no switching behaviour is exhibited. Numerical fittings of the obtained I-V loops indicated that the LRS follows an ohmic conduction mechanism whereas the HRS is governed by the schottky emission effect. The overall switching behaviour in NiO/Nb:STO heterojunction can be explained on the basis of field induced modulation of the interface due to migration of minority charge carriers.

## CHAPTER 7. PROSPECTS FOR FUTURE WORK

### 7.1. Varying the Substrate orientation

Another investigation was undertaken whereby the variance with respect to substrate orientation was examined. The substrate orientation shows a significant impact on the growth of structures (morphology). This is due to the lattice mismatch that occurs between the NiO and STO. Samples were fabricated using the optimised conditions where the temperature, O<sub>2</sub> pressure, pulses, cooling rate and annealing parameters were constant at 900 °C, 50 mTorr, 5 000 pulses, 3 °/min in a vacuum and annealed for 2 hours at 900 °C in 1 Torr O<sub>2</sub> respectively. The substrate orientation was the only parameter changed from STO(001) to STO(111) and STO(110). The aim in this section is to view the nanostructures formed under various substrate orientations and thus determine what the stable structures are. The morphology of these results are shown to be similar to that of Mn<sub>3</sub>O<sub>4</sub> as demonstrated by Bogle *et al.* [7]. A detailed examination of these aspects are planned to be undertaken as part of a doctoral thesis. A brief synopsis of data this far is presented here.

#### 7.1.1. STO (111)

STO (111) was the first substrate orientation under examination. This is portrayed in Figure 7.1.1-1. The SEM image in Figure 7.1.1-1(a) shows no square/rectangle shaped nanostructure formation but a random particle distribution. This is confirmed by the AFM in figure 7.1.1-1(c), which also shows the height of these formations to range from 10-50 nm.

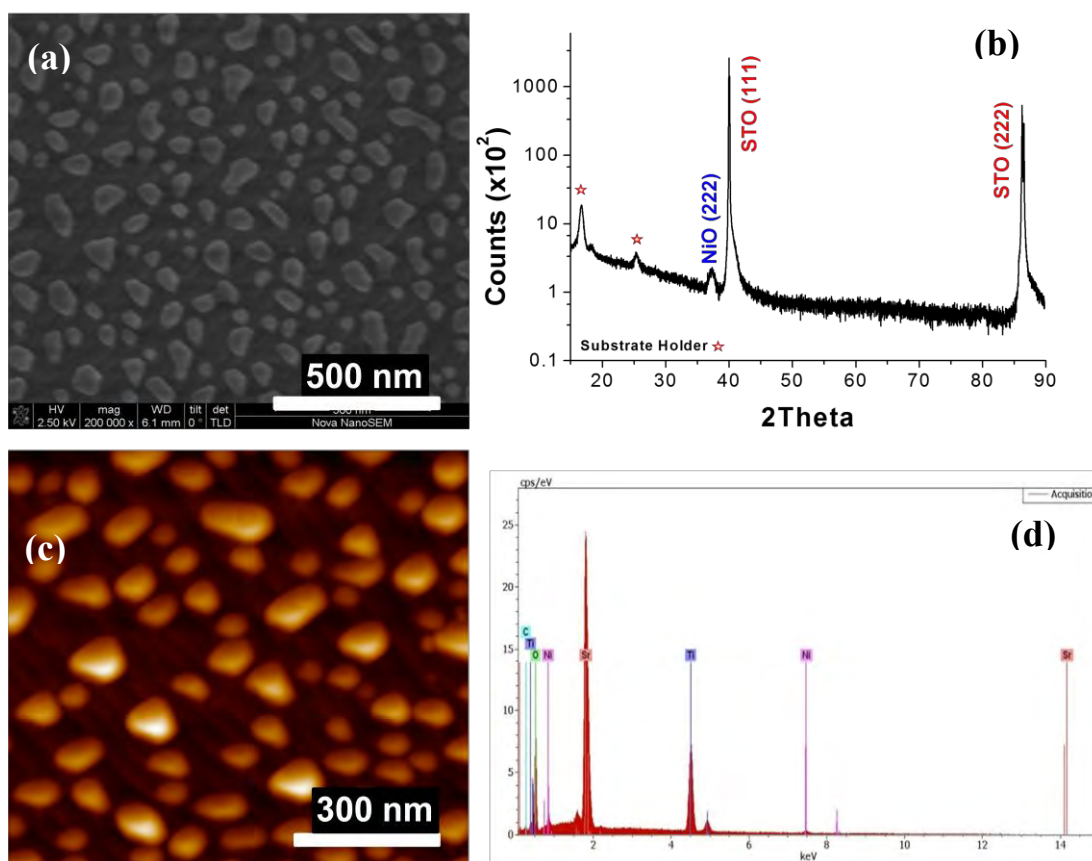


**Figure 7.1.1 -1.** Sample images for depositing in 50 mTorr O<sub>2</sub>, 5 000 pulses, 900 °C and annealing in 1Torr O<sub>2</sub> STO (111) (a) SEM (b) XRD pattern (c) AFM (d) EDS using SEM.

The XRD spectrum of this sample (Figure 7.1.1-1(b)) shows a NiO(222) peak at  $2\theta=37.300$  as well as the STO (111) reflections to prove the sample is also epitaxial. No elemental Bismuth contamination is found in this sample as demonstrated by the EDS images taken using SEM in Figure 7.1.1-1(d).

### 7.1.2. STO (110)

The next sample orientation examined was the STO (110). Figure 7.1.2-1 and 7.1.2-2 shows this data. The SEM image, figure 7.1.2-1(a) displays elongated shaped structures as well as smaller rounded structures. The AFM image in agrees with the SEM image. Analysis via the AFM, figure 7.1.2-1(c) shows the height of the structures to be at approximately 10 nm high. Then looking at the XRD plot in figure 7.1.2-1(b) we see the NiO (220) peak at  $2\theta = 63.121$  and the STO (110) reflections to show that this film is also epitaxial. The TEM image in figure 7.1.2-1(e) shows a magnified view an individual NiO nanostructure at 20nm. This is depicted alongside its diffraction pattern, figure 7.1.2-1(f) which is taken along the (111) zone axis. The orientation of each crystal facet is determined to be (10-1) in the vertical direction and (11-2) in the other. The EDS image shown in figure 7.1.2-1(d) was taken using a TEM and confirms that there are no traces of bismuth (bismuth oxide) in the sample. The peaks that can be seen include the Ni, Sr, Ti and O peaks as well as Ga signal from the holder.

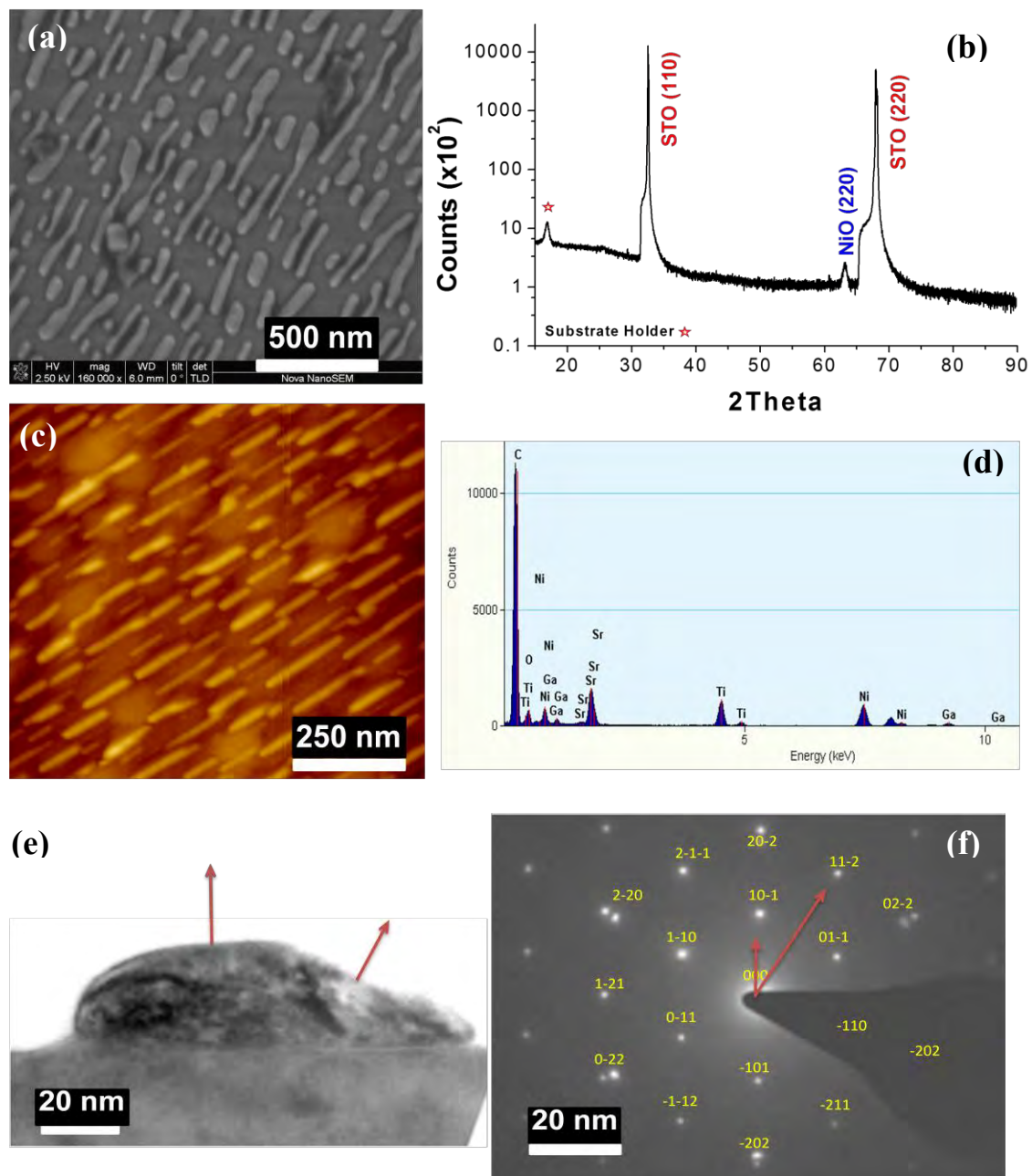


*Figure 7.1.2 -1. Sample images for depositing in 50 mTorr O<sub>2</sub>, 5 000 pulses, 900 °C and annealing in 1Torr O<sub>2</sub> STO (110) (a) SEM (b) XRD pattern (c) AFM.(d) EDS using TEM (e) TEM image of NiO nanostructure (f) electron diffraction pattern.*

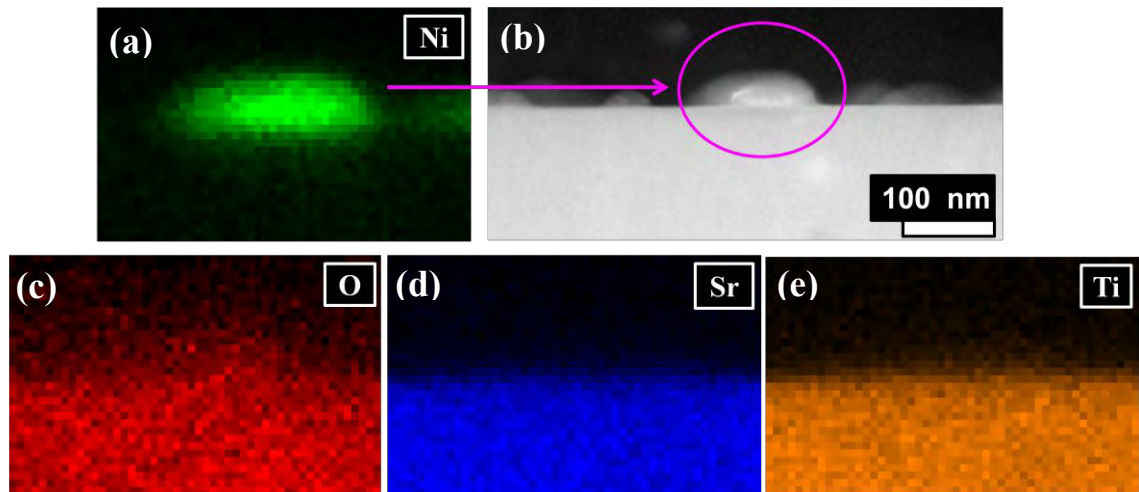


**Figure 7.1.2 -2.** EDS mapping data for (a) Nickel (b) TEM image of NiO nanostructure (c) Strontium (d) Titanate (e) Oxygen.

Figure 7.1.2-2 shows the EDS mapping data for the nanostructure shown in Figure 7.1.2-2(b). Here the composition of the nanostructure is confirmed to be NiO. Figure 7.1.2-2(a) shows the nickel component and Figure 7.1.2-2(c) shows the oxygen contained in the nanostructure as well as the substrate. Figure 7.1.2-2(d) and (e) show the strontium and titanium components contained within the substrate.

## 7.2. Incoherent interface on resistive switching effect

Previous studies [49] on resistive switching memory show the effects of dangling bonds on the resistive switching mechanism (schottky mechanism). Space charges near the electrode are created by dangling bonds (or immobilised free radicals) which then influences the thickness of the interfacial barrier width. This in turn would affect the electronic tunnelling properties. The dangling bonds in the NiO system studied and the effects on the resistive switching properties can be investigated for future work.

## CHAPTER 8. REFERENCES

- [1] S. E. Ahn, M. J. Lee, Y. Park, B. S. Kang, C. B. Lee, K. H. Kim, S. Seo, D. S. Suh, D. C. Kim, and J. Hur, "Write Current Reduction in Transition Metal Oxide Based Resistance Change Memory," *Advanced Materials*, **20**[5] 924-28 (2008).
- [2] A. A. Ansari, M. Alhoshan, M. Alsalhi, and A. Aldwayyan, "Nanostructured Metal Oxides Based Enzymatic Electrochemical Biosensors," *Intelligent and Biosensors* (2010).
- [3] A. Azens, L. Kullman, G. Vaivars, H. Nordborg, and C. Granqvist, "Sputter-Deposited Nickel Oxide for Electrochromic Applications," *Solid State Ionics*, **113** 449-56 (1998).
- [4] A. N. Banerjee and K. K. Chattopadhyay, "Recent Developments in the Emerging Field of Crystalline P-Type Transparent Conducting Oxide Thin Films," *Progress in Crystal Growth and Characterization of Materials*, **50**[1-3] 52-105 (2005).
- [5] G. Binnig, C. F. Quate, and C. Gerber, "Atomic Force Microscope," *Physical Review Letters*, **56**[9] 930 (1986).
- [6] G. Blann and G. Lucas, "Advances in Microstructural Analysis Using Resin Bonded Diamond Surfaces," *Microscopy and Microanalysis*, **10**[SupplementS02] 746-47 (2004).
- [7] K. A. Bogle, V. Anbusathaiah, M. Arredondo, J.-Y. Lin, Y.-H. Chu, C. O'Neill, J. M. Gregg, M. R. Castell, and V. Nagarajan, "Synthesis of Epitaxial Metal Oxide Nanocrystals Via a Phase Separation Approach," *ACS Nano*, **4**[9] 5139-46 (2010).

- [8] K. A. Bogle, M. N. Bachhav, M. S. Deo, N. Valanoor, and S. B. Ogale, "Enhanced Nonvolatile Resistive Switching in Dilutely Cobalt Doped  $\text{TiO}_2$ ," *Applied Physics Letters*, **95** 203502 (2009).
- [9] J. Bohandy, B. F. Kim, and F. J. Adrian, "Metal Deposition from a Supported Metal Film Using an Excimer Laser," *Journal of Applied Physics*, **60** 1538 (1986).
- [10] C. R. Brundle, C. A. Evans, and S. Wilson, "Encyclopedia of Materials Characterization: Surfaces, Interfaces, Thin Films." Gulf Professional Publishing, (1992).
- [11] F. Buatier de Mongeot, W. Zhu, A. Molle, R. Buzio, C. Boragno, U. Valbusa, E. G. Wang, and Z. Zhang, "Nanocrystal Formation and Faceting Instability in  $\text{Al}(110)$  Homoepitaxy: True Upward Adatom Diffusion at Step Edges and Island Corners," *Physical Review Letters*, **91**[1] 016102 (2003).
- [12] X. Chen, X. Hu, and J. Feng, "Nanostructured Nickel Oxide Films and Their Electrochromic Properties," *Nanostructured Materials*, **6**[1-4] 309-12 (1995).
- [13] S. Chikazumi and C. D. Graham, "Physics of Ferromagnetism." Oxford University Press, USA, (1997).
- [14] B. Choi, D. Jeong, S. Kim, C. Rohde, S. Choi, J. Oh, H. Kim, C. Hwang, K. Szot, and R. Waser, "Resistive Switching Mechanism of  $\text{TiO}_2$  Thin Films Grown by Atomic-Layer Deposition," *Journal of applied physics*, **98** 033715 (2005).
- [15] J. S. Choi, J.-S. Kim, I. R. Hwang, S. H. Hong, S. H. Jeon, S.-O. Kang, B. H. Park, D. C. Kim, M. J. Lee, and S. Seo, "Different Resistance Switching Behaviors of  $\text{NiO}$  Thin Films Deposited on Pt and  $\text{SrRuO}_3$  Electrodes," *Applied Physics Letters*, **95**[2] 022109 (2009).

- [16] W. Choi, W. Chim, C. Heng, L. Teo, V. Ho, V. Ng, D. Antoniadis, and E. Fitzgerald, "Observation of Memory Effect in Germanium Nanocrystals Embedded in an Amorphous Silicon Oxide Matrix of a Metal–Insulator–Semiconductor Structure," *Applied physics letters*, **80** 2014 (2002).
- [17] D. Chrisey and G. Hubler, "Pulsed Laser Deposition of Thin Films," *Applied Physics* (2003).
- [18] D. Criswell and R. Waldron, "International Lunar Base and Lunar-Based Power System to Supply Earth with Electric Power," *Acta Astronautica*, **29**[6] 469-80 (1993).
- [19] B. D. Cullity and S. R. Stock, "Elements of X-Ray Diffraction," **Vol. 2**. Addison-Wesley Reading, MA, (1978).
- [20] N. Du, H. Zhang, B. Chen, X. Ma, Z. Liu, J. Wu, and D. Yang, "Porous Indium Oxide Nanotubes: Layer-by-Layer Assembly on Carbon-Nanotube Templates and Application for Room-Temperature  $\text{NH}_3$  Gas Sensors," *Advanced Materials*, **19**[12] 1641-45 (2007).
- [21] R. Eason, "Pulsed Laser Deposition of Thin Films: Applications-Led Growth of Functional Materials." John Wiley & Sons, Inc., (2007).
- [22] M. A. El Khakani, R. Dolbec, A. M. Serventi, M. C. Horrillo, M. Trudeau, R. G. Saint-Jacques, D. G. Rickerby, and I. Sayago, "Pulsed Laser Deposition of Nanostructured Tin Oxide Films for Gas Sensing Applications," *Sensors and Actuators B: Chemical*, **77**[1-2] 383-88 (2001).
- [23] I. Fasaki, A. Giannoudakos, M. Stamataki, M. Kompitsas, E. Gyorgy, I. N. Mihailescu, F. Roubani-kalantzopoulou, A. Lagoyannis, and S. Harissopulos, "Nickel Oxide Thin Films Synthesized by Reactive Pulsed Laser

- Deposition: Characterization and Application to Hydrogen Sensing," *Applied Physics A* (2008).
- [24] J. Feinleib and D. Adler, "Band Structure and Electrical Conductivity of Nio," *Physical Review Letters*, **21**[14] 1010-13 (1968).
- [25] M. Fernández-García and J. A. Rodriguez, "Metal Oxide Nanoparticles," *Encyclopedia of Inorganic and Bioinorganic Chemistry* (2007).
- [26] L. Freund and S. Suresh, "Thin Film Materials: Stress, Defect Formation, and Surface Evolution." Cambridge Univ Pr, (2003).
- [27] J. Gibbons and W. Beadle, "Switching Properties of Thin Nio Films," *Solid-State Electronics*, **7**[11] 785-90 (1964).
- [28] D. A. Glocker, "Handbook of Thin Film Process Technology " **Vol. 2** (2002).
- [29] J. Goldstein, "Scanning Electron Microscopy and X-Ray Microanalysis," **Vol. 1**. Springer Us, (2003).
- [30] K. Gonsalves, "Biomedical Nanostructures." Wiley-Interscience, (2008).
- [31] J. A. Greer and M. D. Tabat, "Large - Area Pulsed Laser Deposition: Techniques and Applications," *American Vacuum Society*, **13**[3] 1 - 7 (1995).
- [32] J. H. Hafner, C. L. Cheung, A. T. Woolley, and C. M. Lieber, "Structural and Functional Imaging with Carbon Nanotube Afm Probes," *Progress in Biophysics and Molecular Biology*, **77**[1] 73-110 (2001).
- [33] C. G. Harman and B. W. King, "Applications of Nickel Compounds in Ceramics," *Industrial & Engineering Chemistry*, **44**[5] 1015-17 (1952).
- [34] B. B. He, "Two-Dimensional X-Ray Diffraction." John Wiley & Sons Inc, (2009).
- [35] J. H. Hsu, H. W. Lai, H. N. Lin, C. C. Chuang, and J. H. Huang, "Fabrication of Nickel Oxide Nanostructures by Atomic Force Microscope Nano-Oxidation and

- Wet Etching," *Journal of Vacuum Science & Technology B: Microelectronics and Nanometer Structures*, **21** 2599 (2003).
- [36] L. Huang, B. Qu, L. Liu, and L. Zhang, "Study on the Resistive Switching Properties of Epitaxial La<sub>0.67</sub>Sr<sub>0.33</sub>MnO<sub>3</sub> Films," *Solid state communications*, **143**[8-9] 382-85 (2007).
- [37] A. W. Hull, "A New Method of Chemical Analysis," *Journal of the American Chemical Society*, **41**[8] 1168-75 (1919).
- [38] H. Hwang, J. Song, and T. Susaki, "Enhanced Thermodynamic Stability of Epitaxial Oxide Thin Films," *Advanced Materials*, **20**[13] 2528-32 (2008).
- [39] I. Hwang, J. Choi, S. Hong, J. S. Kim, I. S. Byun, J. H. Bahng, J. Y. Koo, S. O. Kang, and B. H. Park, "Direct Investigation on Conducting Nanofilaments in Single-Crystalline Ni/NiO Core/Shell Nanodisk Arrays," *Applied Physics Letters*, **96** 053112 (2010).
- [40] M. D. Irwin, D. B. Buchholz, A. W. Hains, R. P. H. Chang, and T. J. Marks, "P-Type Semiconducting Nickel Oxide as an Efficiency-Enhancing Anode Interfacial Layer in Polymer Bulk-Heterojunction Solar Cells," *Proceedings of the National Academy of Sciences*, **105**[8] 2783-87 (2008).
- [41] D. S. Jeong, "Resistive Switching in Pt/TiO<sub>2</sub>/Pt," **Vol. 6**. Forschungszentrum Jülich, (2008).
- [42] D. P. Joseph, M. Saravanan, B. Muthuraaman, P. Renugambal, S. Sambasivam, S. P. Raja, P. Maruthamuthu, and C. Venkateswaran, "Spray Deposition and Characterization of Nanostructured Li Doped NiO Thin Films for Application in Dye-Sensitized Solar Cells," *Nanotechnology*, **19**[48] 485707 (2008).

- [43] K. M. Kim, B. J. Choi, and C. S. Hwang, "Localized Switching Mechanism in Resistive Switching of Atomic-Layer-Deposited TiO<sub>2</sub> Thin Films," *Applied Physics Letters*, **90**[24] 242906 (2007).
- [44] P. Kislyi and M. Kuzenkova, "Evaluation of the Surface Energy of Some Metals and Refractory Compounds," *Powder Metallurgy and Metal Ceramics*, **8**[10] 809-12 (1969).
- [45] H. Kohlstedt, A. Petraru, K. Szot, A. Rudiger, P. Meuffels, H. Haselier, R. Waser, and V. Nagarajan, "Method to Distinguish Ferroelectric from Nonferroelectric Origin in Case of Resistive Switching in Ferroelectric Capacitors," *Applied Physics Letters*, **92**[6] 062907 (2008).
- [46] R. V. Kumar, Y. Diamant, and A. Gedanken, "Sonochemical Synthesis and Characterization of Nanometer-Size Transition Metal Oxides from Metal Acetates," *Chemistry of Materials*, **12**[8] 2301-05 (2000).
- [47] D.-H. Kwon, K. M. Kim, J. H. Jang, J. M. Jeon, M. H. Lee, G. H. Kim, X.-S. Li, G.-S. Park, B. Lee, S. Han, M. Kim, and C. S. Hwang, "Atomic Structure of Conducting Nanofilaments in TiO<sub>2</sub> Resistive Switching Memory," *Nat Nano*, **5**[2] 148-53 (2010).
- [48] J. Lee, M. Ortolani, U. Schade, Y. Chang, and T. Noh, "Microspectroscopic Detection of Local Conducting Areas Generated by Electric-Pulse-Induced Phase Transition in VO Films," *Applied Physics Letters*, **91** 133509 (2007).
- [49] M. H. Lee and C. S. Hwang, "Resistive Switching Memory: Observations with Scanning Probe Microscopy," *Nanoscale*, **3**[2] 490-502 (2011).
- [50] M. J. Lee, Y. Park, D. S. Suh, E. H. Lee, S. Seo, D. C. Kim, R. Jung, B. S. Kang, S. E. Ahn, and C. Lee, "Two Series Oxide Resistors Applicable to High Speed

- and High Density Nonvolatile Memory," *Advanced Materials*, **19**[22] 3919-23 (2007).
- [51] S. R. Lee, K. Char, D. C. Kim, R. Jung, S. Seo, X. Li, G. S. Park, and I. Yoo, "Resistive Memory Switching in Epitaxially Grown NiO," *Applied Physics Letters*, **91** 202115 (2007).
- [52] J. G. Lu, P. Chang, and Z. Fan, "Quasi-One-Dimensional Metal Oxide Materials-Synthesis, Properties and Applications," *Materials Science and Engineering: R: Reports*, **52**[1-3] 49-91 (2006).
- [53] Q. Lu, F. Gao, and S. Komarneni, "Multi-Level Assemblies of Lead Sulphide Nanorods," *Nanotechnology*, **17** 2574 (2006).
- [54] Magnetization.Dynamics.Group, "Pulsed Laser Deposition System." in Department of physics. Colorado State University, Colorado, 2008.
- [55] M. S. J. Marshall and M. R. Castell, "Shape Transitions of Epitaxial Islands During Strained Layer Growth: Anatase TiO<sub>2</sub>(001) on SrTiO<sub>3</sub>(001)," *Physical Review Letters*, **102**[14] 146102 (2009).
- [56] G. Mattei, P. Mazzoldi, M. L. Post, D. Buso, M. Guglielmi, and A. Martucci, "Cookie-Like Au/NiO Nanoparticles with Optical Gas-Sensing Properties," *Advanced Materials*, **19**[4] 561-64 (2007).
- [57] D. Mattox, "Handbook of Physical Vapor Deposition (Pvd) Processing: Film Formation, Adhesion, Surface Preparation and Contamination Control." William Andrew Publishing, (1998).
- [58] Merck13, "NiO." in, **Vol. 6536**. Merck Chemicals Australia, 2010.
- [59] K. C. Min, M. Kim, Y. H. You, S. Lee, Y. Lee, T. M. Chung, C. Kim, J. H. Hwang, K. S. An, and N. S. Lee, "NiO Thin Films by MOCVD of Ni (DMAMB) 2

- and Their Resistance Switching Phenomena," *Surface and Coatings Technology*, **201**[22-23] 9252-55 (2007).
- [60] I. Mowat, J. Moskito, I. Ward, and A. Hartzell, "Analytical Methods for Nanotechnology," *Evans Analytical Group, US* (2007).
- [61] R. S. Muller, T. I. Kamins, M. Chan, and P. K. Ko, "Device Electronics for Integrated Circuits." John Wiley & Sons., (1986).
- [62] R. Newman and R. M. Chrenko, "Optical Properties of Nickel Oxide," *Physical Review*, **114**[6] 1507 (1959).
- [63] D. P. Norton, "Synthesis and Properties of Epitaxial Electronic Oxide Thin-Film Materials," *Materials Science and Engineering: R: Reports*, **43**[5-6] 139-247 (2004).
- [64] K. Oka, T. Yanagida, K. Nagashima, H. Tanaka, and T. Kawai, "Nonvolatile Bipolar Resistive Memory Switching in Single Crystalline NiO Heterostructured Nanowires," *Journal of the American Chemical Society*, **131**[10] 3434-35 (2009).
- [65] D. Paul Joseph, M. Saravanan, B. Muthuraaman, P. Renugambal, S. Sambasivam, S. Philip Raja, P. Maruthamuthu, and C. Venkateswaran, "Spray Deposition and Characterization of Nanostructured Li Doped NiO Thin Films for Application in Dye-Sensitized Solar Cells," *Nanotechnology*, **19** 485707 (2008).
- [66] H. Y. Peng, G. P. Li, J. Y. Ye, Z. P. Wei, Z. Zhang, D. D. Wang, G. Z. Xing, and T. Wu, "Electrode Dependence of Resistive Switching in Mn-Doped ZnO: Filamentary Versus Interfacial Mechanisms," *Applied Physics Letters*, **96**[19] 192113 (2010).
- [67] M. Porti, M. Nafria, X. Aymerich, A. Olbrich, and B. Ebersberger, "Electrical Characterization of Stressed and Broken Down SiO<sub>2</sub> Films at a Nanometer Scale

- Using a Conductive Atomic Force Microscope," *Journal of Applied Physics*, **91** 2071 (2002).
- [68] P. Qin, M. Linder, T. Brinck, G. Boschloo, A. Hagfeldt, and L. Sun, "High Incident Photon-to-Current Conversion Efficiency of P-Type Dye-Sensitized Solar Cells Based on NiO and Organic Chromophores," *Advanced Materials*, **21**[29] 2993-96 (2009).
- [69] M. Sánchez, M. Rozenberg, and I. Inoue, "A Mechanism for Unipolar Resistance Switching in Oxide Nonvolatile Memory Devices," *Applied physics letters*, **91**[25] 252101 (2007).
- [70] B. Sasi and K. G. Gopchandran, "Nanostructured Mesoporous Nickel Oxide Thin Films" *Nanotechnology*, **18**[11] 1 - 9 (2007).
- [71] K. D. Sattler, "Nanotubes and Nanowires." CRC, (2010).
- [72] A. Sawa, "Resistive Switching in Transition Metal Oxides," *Materials Today*, **11**[6] 28-36 (2008).
- [73] S. Seo, M. Lee, D. Seo, S. Choi, D. S. Suh, Y. Joung, I. Yoo, I. Byun, I. Hwang, and S. Kim, "Conductivity Switching Characteristics and Reset Currents in NiO Films," *Applied Physics Letters*, **86** 093509 (2005).
- [74] K. Shibuya, R. Dittmann, S. Mi, and R. Waser, "Impact of Defect Distribution on Resistive Switching Characteristics of SrTiO<sub>3</sub> Thin Films," *Advanced Materials*, **22**[3] 411-14 (2010).
- [75] H. Shima, F. Takano, H. Akinaga, Y. Tamai, I. H. Inoue, and H. Takagi, "Resistance Switching in the Metal Deficient-Type Oxides: NiO and CoO," *Applied Physics Letters*, **91** 012901 (2007).

- [76] F. Silly and M. R. Castell, "Selecting the Shape of Supported Metal Nanocrystals: Pd Huts, Hexagons, or Pyramids on  $\text{SrTiO}_3(001)$ ," *Physical Review Letters*, **94**[4] 046103 (2005).
- [77] S. Soeya, M. Fuyama, S. Tadokoro, and T. Imagawa, "NiO Structure-Exchange Anisotropy Relation in the  $\text{Ni}_{81}\text{Fe}_{19}/\text{NiO}$  Films and Thermal Stability of Its NiO Film," *Journal of Applied Physics*, **79**[3] 1604-10 (1996).
- [78] P. Song, D. Wen, Z. X. Guo, and T. Korakianitis, "Oxidation Investigation of Nickel Nanoparticles," *Physical Chemistry Chemical Physics*, **10**[33] 5057 (2008).
- [79] C. Suryanarayana and M. G. Norton, "X-Ray Diffraction: A Practical Approach," **Vol. 4**. Cambridge Univ Press, (1998).
- [80] K. Szot, W. Speier, G. Bihlmayer, and R. Waser, "Switching the Electrical Resistance of Individual Dislocations in Single-Crystalline  $\text{SrTiO}_3$ ," *Nature Materials*, **5**[4] 312-20 (2006).
- [81] R. K. Vasudevan, Y.-C. Chen, H.-H. Tai, N. Balke, P. Wu, S. Bhattacharya, L. Q. Chen, Y.-H. Chu, I. N. Lin, S. V. Kalinin, and V. Nagarajan, "Exploring Topological Defects in Epitaxial  $\text{BiFeO}_3$  Thin Films," *ACS Nano*, **5**[2] 879-87 (2011).
- [82] L. Vayssieres, "Growth of Arrayed Nanorods and Nanowires of ZnO from Aqueous Solutions," *Advanced Materials*, **15**[5] 464-66 (2003).
- [83] T. Venkatesan, X. D. Wu, A. Inam, and J. B. Wachtman, "Observation of Two Distinct Components During Pulsed Laser Deposition of High  $T_c$  Superconducting Films," *Applied Physics Letters*, **52**[14] 1193-95 (1988).

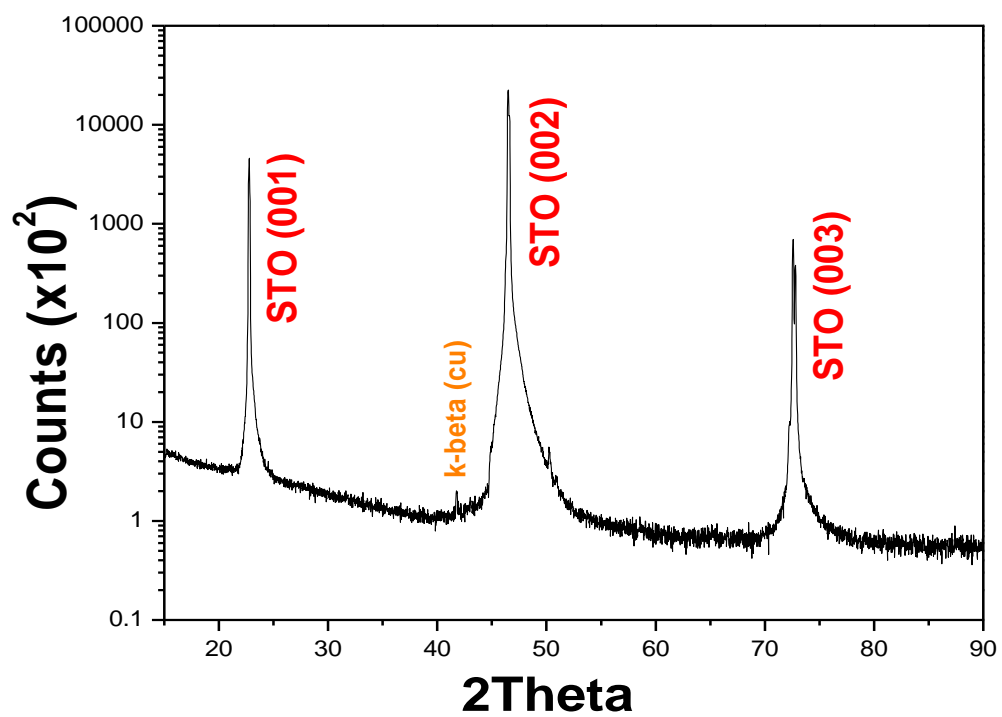
- [84] J. Wang, H. Pang, J. Yin, L. Guan, Q. Lu, and F. Gao, "Controlled Fabrication and Property Studies of Nickel Hydroxide and Nickel Oxide Nanostructures," *CrystEngComm*, **12**[5] 1404-09 (2010).
- [85] R. Waser and M. Aono, "Nanoionics-Based Resistive Switching Memories," *Nature Materials*, **6**[11] 833-40 (2007).
- [86] R. O. Wayne, "Light and Video Microscopy." Academic Press, (2008).
- [87] Z. P. Wei, M. Arredondo, H. Y. Peng, Z. Zhang, D. L. Guo, G. Z. Xing, Y. F. Li, L. M. Wong, S. J. Wang, and N. Valanoor, "A Template and Catalyst-Free Metal-Etching-Oxidation Method to Synthesize Aligned Oxide Nanowire Arrays: NiO as an Example," *ACS nano* (2010).
- [88] D. B. Williams and C. B. Carter, "The Transmission Electron Microscope," *Transmission Electron Microscopy* 3-22 (2009).
- [89] M. Winter, "Web Elements. Nickel Oxide." in, **Vol. 2010**. The University of Sheffield Sheffield, UK, 2010.
- [90] W. L. Winterbottom, "Equilibrium Shape of a Small Particle in Contact with a Foreign Substrate," *Acta Metallurgica*, **15**[2] 303-10 (1967).
- [91] M.-S. Wu, Y.-A. Huang, C.-H. Yang, and J.-J. Jow, "Electrodeposition of Nanoporous Nickel Oxide Film for Electrochemical Capacitors," *International Journal of Hydrogen Energy*, **32**[17] 4153-59 (2007).
- [92] X. Wu, P. Zhou, J. Li, L. Chen, H. Lv, Y. Lin, and T. Tang, "Reproducible Unipolar Resistance Switching in Stoichiometric ZnO Films," *Applied Physics Letters*, **90**[18] 183507-07-3 (2007).
- [93] H. Yang, H. M. Luo, H. Wang, I. O. Usov, N. A. Suvorova, M. Jain, D. M. Feldmann, P. C. Dowden, R. F. DePaula, and Q. X. Jia, "Rectifying Current-

Voltage Characteristics of Bifeo[Sub 3]/Nb-Doped Sr tio[Sub 3]  
Heterojunction," *Applied Physics Letters*, **92**[10] 102113 (2008).

- [94] J. B. Yi, J. Ding, Y. P. Feng, G. W. Peng, G. M. Chow, Y. Kawazoe, B. H. Liu, J. H. Yin, and S. Thongmee, "Size-Dependent Magnetism and Spin-Glass Behavior of Amorphous NiO Bulk, Clusters, and Nanocrystals: Experiments and First-Principles Calculations," *Physical Review B*, **76**[22] 224402 (2007).
- [95] Y.-P. Zhao, D.-X. Ye, G.-C. Wang, and T.-M. Lu, "Designing Nanostructures by Glancing Angle Deposition," *Proceedings of SPIE*, **5219**[59] 59-73 (2003).
- [96] W. Zhu, F. Buatier de Mongeot, U. Valbusa, E. G. Wang, and Z. Zhang, "Adatom Ascending at Step Edges and Faceting on Fcc Metal (110) Surfaces," *Phys. Rev. Lett.*, **92**[10] 106102 (2004).
- [97] J. M. Zuo and J. C. Mabon, "Web-Based Electron Microscopy Application Software: Web-Emaps, Microsc Microanal 10(Suppl 2)." in., 2004.

## APPENDICES

### APPENDIX A – Blank STO (substrate) XRD peaks



**APPENDIX B – Substrate holder XRD peaks**

